Multiphoton Ionization Spectroscopy of $AlAr_N$ Clusters†

J. M. Spotts,‡ C.-K. Wong, M. S. Johnson,§ and M. Okumura

Arthur Amos Noyes Laboratory of Chemical Physics, California Institute of Technology, MS 127-72, Pasadena, California 91125-0001

J. A. Boatz, R. J. Hinde,⊥ J. A. Sheehy,|| and P. W. Langhoff*

Air Force Research Laboratory, 10 East Saturn Drive, Edwards Air Force Base, California 93524-7680

Received: March 31, 2003; In Final Form: June 5, 2003

Experimental and theoretical studies are reported of the multiphoton ionization spectroscopy of selected $AlAr_N$ clusters ($N = 2-54$). Resonantly enhanced $1_{uv} + 1_{vis}$ and $2_{vis} + 1_{vis}$ ionization spectra are recorded of neutral clusters employing a laser-ablation/pulsed supersonic expansion source and time-of-flight mass spectrometric cluster-ion detection. The spectra are dominated by broad red- and blue-shifted asymmetric bands in the neighborhood of the 308 and 303 nm atomic Al 3p → 3d and 4p lines. The detailed structures of these bands and the observed degree of their spectral shifts with increasing cluster size are attributed on the basis of concomitant ab initio theoretical calculations to interplay among a number of factors, including (i) the comparable strengths of spin−orbit-split anisotropic $(^2P_{1/2})Al-(^1S_0)Ar$ interactions and Ar−Ar mutual attractions, responsible for predicted external-site Al atom locations on distorted icosahedral Ar_N structures, (ii) avoided crossings in the nearly degenerate $AlAr_N$ potential energy surfaces accessed by one- and two-photon atomic Al 3p → 3d and 4p excitations, giving rise to the red- and blue-shifted spectral profiles, and (iii) significant dynamical rearrangement and parent cluster-ion fragmentation following ionization, resulting in Al^+Ar_M signals that generally reflect the absorption cross sections of an ensemble of larger prior clusters ($AlAr_N$, $N > M$). Additionally, nonuniformity in the cluster-size distribution of the incident molecular beam is inferred from the calculated and measured spectra and must be incorporated in the development for a completely satisfactory accounting between theory and experiment. Comparisons with the results of earlier experimental studies of the ionization potentials of $AlAr_N$ clusters also underscore the importance of dynamical parent-ion rearrangement and fragmentation, consequent of the increased Ar solvation of the Al^+ radical in the equilibrium Al^+Ar_M cluster-ion structures. The reported multiphoton ionization cluster-ion spectra are evidently highly sensitive to the details of the atomic Ar arrangements around the Al chromophore and accordingly provide a spectroscopic probe of the nature and evolution of the Al trapping sites and cluster geometries with increasing cluster size when the complex electronic and vibrational phenomena underlying the measurements are appropriately interpreted.

1. Introduction

Radical species have long been profitably studied spectroscopically in cryogenic hosts.[1−3] The ultraviolet absorption, magnetic circular dichroism, and electron spin-resonance spectra of Al atoms trapped in rare-gas matrixes,[4−8] liquids,[9] and finite cryogenic clusters,[10−13] in particular, have been subjects of continuing fundamental interest and have also attracted attention in connection with development of high-specific-impulse cryogenic fuels under the auspices of the United States Air Force (USAF) high-energy density matter program.[14,15] To describe comprehensively the structures and spectra of trapped open p-shell radicals, corresponding interpretive theoretical studies must incorporate the effects of spin−orbit splittings and the noncentral spatially anisotropic natures of the Al atom interactions with the cryogenic host material in both ground and excited electronic states. Combined theoretical and experimental studies of Al-doped cryogenic hosts can provide an opportunity to understand the evolution of the many factors that contribute to measured spectral shifts with increasing degree of solvation in such systems, particularly the natures of the atomic Al trapping sites that give rise to the observed spectroscopic behaviors.

The previously reported atomic Al matrix-isolation absorption spectra have revealed large blue shifts (∼50 nm) of the 395 nm 3p → 4s resonance line in solid Ar[4−7] and Kr[8] and in liquid He.[9] In contrast, the 308 nm atomic 3p → 3d line apparently gives rise to somewhat smaller blue shifts (∼20 nm) but is split over a broad spectral range (∼40 nm) in the matrix.[4−8] Such prominent spectral shifts to the blue suggest that a largely repulsive interaction in the spatially extended excited electronic

† Work supported in part by grants from the U. S. Air Force Office of Scientific Research.

* To whom correspondence should be addressed. Present address: San Diego Supercomputer Center, University of California, 9500 Gilman Drive, La Jolla, CA, 92093-0505. E-mail: langhoff@drifter.sdsc.edu. Fax: 858-822-5407. Phone: 858-822-3611.

‡ Present address: Department of Neuroscience, Children's Hospital, 260 John F. Enders Pediatric Laboratories, Harvard Medical School, 300 Longwood Avenue, Boston, MA 02115.

§ Present address: Department of Chemistry, University of Copenhagen, Universitetsparken 5, DK-2100 Copenhagen Ø, Denmark.

⊥ Present address: Department of Chemistry, University of Tennessee, Knoxville, TN 37996-1600.

|| Present address: Propulsion Research Center (TD-40), NASA Marshall Space Flight Center, Huntsville, AL 35812.

10.1021/jp030399o CCC: $25.00
Published on Web 08/15/2003

state complements the stabilization provided by the rare-gas solvation of the more compact ground electronic state. Strongly blue-shifted spectral profiles are also reported in studies of Al 3p → 4s and other excitations in solid H_2[14] and of 3p → 3d excitation in finite He clusters, which exhibit significant nonradiative decay into the fluorescent 4s state.[12] The latter observations are in accord with Al fluorescence quenching in liquid He[9] and with observations of 4s fluorescence following 3p → 3d excitation in the Al−H_2 van der Waals complex.[13]

In contrast to the large (3p → 4s and 3d) atomic Al spectral shifts observed in solid Ar,[4−7] spectroscopic studies of size-selected $AlAr_N$ clusters indicate that the 3p → 4s atomic Al line is shifted incrementally with increasing cluster size by only ∼5−15 nm to the blue for clusters ranging from $N = 1$ to 28 Ar atoms, with some degree of spectral structure reported.[10,11] Observations of these relatively small blue shifts, which appear to converge with increasing N to only ∼50% of the value observed in Ar matrixes,[4−7] suggest that the cluster trapping sites differ from those of the matrix-isolated studies, possibly involving atomic Al locations external to the clusters[15] or an internal site not typical of the bulk phase.[16] The trend in the measured $AlAr_N$ cluster-ion appearance potentials, which does not show convergence with increasing cluster size to the bulk-value predictions of continuum dielectric polarization theories,[11] also contributes to the ambiguous nature of the Al trapping sites in Ar cluster hosts.

Although several studies have suggested that metal dopants in rare-gas clusters often lie on the surface of the cluster (e.g., alkali metal species on liquid He droplets[17] or B atoms on Ar_N clusters[18]), Al might be expected to be fully solvated in Ar clusters because the well depth and equilibrium bond length of the ground-state $^2\Pi_{1/2}$ Al−Ar potential curve ($D_e = 122.4$ cm^{-1}, $R_e = 3.79$ Å)[19] are similar to those of the Ar−Ar potential ($D_e = 99$ cm^{-1}, $R_e = 3.76$ Å).[20] Previous attempts to model $AlAr_N$ clusters, however, have either employed an isotropic potential,[11,16] or apparently studied only $AlAr_{12}$ structures that correspond to local minima in the neighborhood of an Al-centered icosahedral cluster employing simulated annealing in an anisotropic (elliptical) external potential.[21] As a consequence, the ground-state geometry of neutral $AlAr_N$ clusters more generally remains uncertain at present.

In view of the likely sensitivity of the ground-state structures of $AlAr_N$ clusters to anisotropic and spin−orbit splitting in Al−Ar interactions and of the corresponding sensitivity of their ultraviolet excitation spectra to trapping site geometries, resonant multiphoton ionization spectra of these open-shell clusters can provide a means, in principle, of studying the evolution of trapping sites and their associated verifiable physical consequences with increasing degree of solvation. The interpretation of such spectra suffers from several difficulties, however, including (i) uncertainties in the initial ground-state cluster geometry and the possible existence of thermally accessible isomers, (ii) ambiguity in assigning electronic bands to open-shell excited states, especially when the initial geometry is not known, (iii) the likelihood of extensive cluster fragmentation, especially upon ionization, and (iv) the existence of other photophysical pathways that may compete with ionization.

In the present article, systematic joint experimental and theoretical studies are reported of multiphoton ionization spectra of $AlAr_N$ ($N = 2−54$) clusters in a combined effort to characterize their structures and the physical origins of the size-dependent spectra observed. Particular emphasis is placed on the Al 3p → 3d and 4p spectral profiles observed in size-selected Ar clusters, which are expected to be particularly sensitive to cluster geometry through the strong interactions among these nearly degenerate states. The experiments employ a laser-ablation/pulsed molecular-beam cluster source, resonant $1_{uv} + 1_{vis}$ and $2_{vis} + 1_{vis}$ multiphoton ionization, and time-of-flight mass spectrometric cluster-ion detection, as described in section 2. The theoretical studies include the aforementioned spin−orbit splittings and anisotropic electronic interactions in determinations of the cluster ground-state geometries and electronic excitation spectra, as well as classical Monte Carlo calculations of the vibrational degrees of freedom in the ground and electronically excited states. Additionally, vertical and adiabatic ionization potentials and the ground-state geometries of the cluster ions are reported, and molecular dynamics simulations of the rearrangements and fragmentation patterns in the parent-ion clusters are performed employing diffusion quantum Monte Carlo initial conditions, as described in section 3.

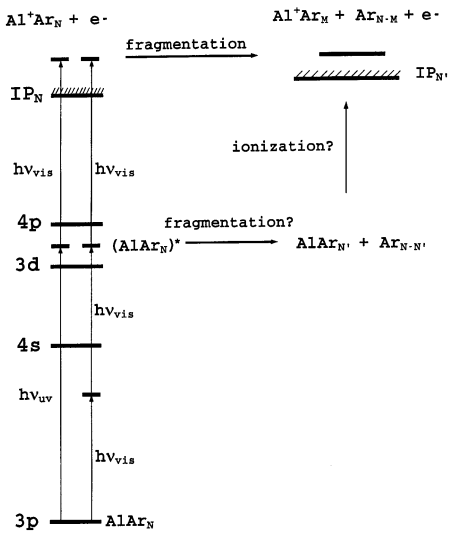

Figure 1. Schematic representation of the $AlAr_N$ resonant $1_{uv} + 1_{vis}$ and $2_{vis} + 1_{vis}$ one-color multiphoton ionization processes for production of Al^+Ar_M cluster ions. The rapid sequential vertical (1_{uv} or 2_{vis}) excitation and (1_{vis}) ionization followed by fragmentation of excited Al^+Ar_N cluster ions depicted on the left is assumed to dominate the alternative channel involving fragmentation of excited neutrals ($AlAr_N$*) and their ionization, as well as other weaker channels discussed in the text.

Figure 1 provides a schematic representation of the resonant $1_{uv} + 1_{vis}$ and $2_{vis} + 1_{vis}$ multiphoton ionization of neutral $AlAr_N$ clusters resulting in production of Al^+Ar_M cluster ions ($M \leq N$). The vertical excitation/ionization sequence depicted on the left in the figure, involving sudden electronic excitation and ionization followed by cluster-ion fragmentation, is expected to be the dominant mechanism of ion production. As is discussed in detail below, the significant change in potential energy surface experienced upon cluster ionization results in much greater vibrational excitation and fragmentation of parent cluster ions than that arising from excitation of the neutral clusters. Of course, other weak decay processes that quench the excited electronic states of the neutral clusters can be envisioned, including internal conversion, fluorescence, and intersystem crossings, as well as ejection of the strongly bound Al^+ ion and the associated formation of neutral Ar_N clusters. These and other low probability processes are not depicted in Figure 1 and are not included in the calculations reported here.

The Al^+Ar_M cluster ions arising from the dominant channel depicted in Figure 1 are produced by the indicated sequence of photoexcitation, ionization, and dissociation processes for a range of larger prior clusters $AlAr_N$, each of which can

contribute to a single cluster-ion Al^+Ar_M signal. The mass spectrometric signal for detection of cluster ions Al^+Ar_M on the basis of the $1_{uv} + 1_{vis}$ excitation−ionization mechanism of Figure 1 can be written in the form

$$N_M^{(+)}(h\nu_{uv}) \propto \sum_N P_N \{\sigma_{abs}^{(N)}(h\nu_{uv}) I_{uv}(h\nu_{uv})\}\{\sigma_{ion}^{(N)}(h\nu_{vis}) I_{vis}(h\nu_{vis})\} F_{NM}^{(+)} \quad (1)$$

Here, P_N is the cluster-size distribution of the incident $AlAr_N$ beam, $\sigma_{abs}^{(N)}(h\nu_{uv})$ is the ultraviolet (1_{uv}) photoabsorption cross section of the neutral cluster in its ground state, $I_{uv}(h\nu_{uv})$ is the ultraviolet photon intensity or fluence, $\sigma_{ion}^{(N)}(h\nu_{vis})$ and $I_{vis}(h\nu_{vis})$ are corresponding quantities for ionization of the electronically excited neutral clusters $(AlAr_N)^*$ by visible (1_{vis}) photons, and $F_{NM}^{(+)}$ is the unity-normalized fragmentation probability for production of the cluster ion Al^+Ar_M from the cluster ion $(Al^+Ar_N)^*$ ($M \leq N$). A similar expression not evaluated here is obtained for $2_{vis} + 1_{vis}$ excitation and ionization, where the one-photon absorption cross section and ultraviolet intensity in eq 1 are replaced by corresponding two-photon $[\sigma_{2-photon}^{(N)}(h\nu_{vis})$ and $I_{vis}^2(h\nu_{vis})]$ quantities.

2. Experimental Section

The apparatus employed to generate $AlAr_N$ clusters and its operating characteristics are described in detail elsewhere.[15,22,23] The laser ablation source is a tripled Nd:YAG laser (355 nm, Continuum Surelite 1) focused on a 0.6-cm diameter rotatable 2024 aluminum alloy rod, which produces ablated Al atoms. These are entrained into the leading edge of an expanding Ar gas/cluster mixture produced by a piezoelectric-driven pulsed value, which generates 100−300 μs pulses of Ar carrier gas at stagnation pressures of 8−10 atm into the source vacuum chamber through a 2-mm diameter channel. The ablated Al atoms are introduced at the end of the channel, where it widens to a 90° cone. The resulting jet of Al-seeded Ar clusters in Ar carrier gas passes through a 3-mm diameter orifice skimmer (Beam Dynamics) and is introduced into a differentially pumped photon interaction region. Ions produced in the ablation plasma at ground potential are deflected by the 1−2 kV extraction optics so do not contribute to the measured signals, as is verified directly in the experiment. Rotational temperatures of diatomic AlAr produced in the apparatus are found to be less than ~10 K with no evidence of hot bands present in the spectra[22,23] Although temperatures are not otherwise measured, the diatomic temperatures and a priori energetic considerations suggest a range of ~10−30 K for the larger clusters.

The clusters are excited and ionized by ultraviolet (1_{uv}) and visible (1_{vis}) photons produced by an unfocused Continuum TDL-51 dye laser pumped by the doubled output of a Nd:YAG laser (Continuum NY61-20) propagating nearly collinearly and at right angles to the cluster beam. The ionization signals are detected with a pair of gated integrators set to collect ions with the ablation laser on and off in alternative cycles to allow for subtraction of background ionization. A sequence of dyes and 50%/50% dye mixtures (DCM, 338−304 nm; R640, 315−303 nm; R640/R610, 315−297 nm; R610, 304−291 nm; R610/R590, 315−288 nm; R590, 300−288 nm) spans the wavelength interval of interest. The ultraviolet photons are generated by frequency doubling the dye laser output using KD*P crystals (DCC-2, DCC-3, Continuum), whereas the visible photons are taken from the residual undoubled dye fundamental that exits the doubling crystal coaxially with the ultraviolet laser pulse. In this ($1_{uv} + 1_{vis}$) arrangement, the ultraviolet (~1−4 mJ/pulse) and visible (~10−50 mJ/pulse) photons are scanned together ($\lambda_{vis} = 2\lambda_{uv}$) over the range $\lambda_{uv} \approx 330-290$ nm. In a second arrangement, the fundamental output of the dye laser is focused with a 150 mm focal length lens to drive $2_{vis} + 1_{vis}$ multiphonon ionization of the doped clusters. This approach excites primarily two-photon-allowed intermediate electronic cluster states associated with 3p → 4p Al excitation for comparison with the dipole-allowed 3p → 3d spectra obtained employing single ultraviolet photon excitation. The dye laser fundamental frequency is calibrated in all cases using an atomic sodium D line arc lamp and, when accessible, with the Al atomic transitions detected by the Al^+ multiphoton ionization signal.

Following cluster ionization, the ions are accelerated to ~2 keV and are extracted perpendicularly to the beam and mass-analyzed employing a 1-m Wiley−McLaren time-of-flight mass spectrometer, a chevron dual-microchannel plate detector (Galileo), and a transient digitizer (LeCroy 8818). The path lengths and kinetic energies of cluster ions produced under these conditions result in flight times in the apparatus that are estimated to be ~30 μs for the clusters reported upon here. Individual scans are recorded by isolating the mass peaks of interest with a pair of gated integrators (SR-250, Stanford Research Systems).

To obtain continuous ($1_{uv} + 1_{vis}$) spectra over the full range of dyes employed, the recorded mass-selected cluster-ion signals within each range are normalized to the ultraviolet fluence of the laser pulse [eq 1], providing spectra that do not contain the intensity variations of the incident ultraviolet radiation over the spectral interval reported. At the high visible power levels (~10−50 mJ/pulse ≈ 10^8 photons/cm^2/pulse) employed, the ionization step of Figure 1 and eq 1 is saturated, and the spectral variation of the ionizing visible photon beam and of the photoionization cross section is not contained in the data. The one-color two-photon spectra ($2_{vis} + 1_{vis}$) reported are similarly normalized to the visible exciting and ionizing radiation employing a separate power-dependence scan. In the $1_{uv} + 1_{vis}$ experiments, the power dependence is found to be strictly linear in I_{uv}, whereas in the $2_{vis} + 1_{vis}$ experiments, the dependence is typically ~$I_{vis}^{2.6}$. The final complete action spectra are assembled from the results in the individual laser dye intervals by matching the amplitudes of the adjacent data sets in the regions of overlapping wavelengths.

3. Theoretical Section

Interpretations of the measured multiphoton spectra are based on results obtained from a concomitant theoretical study incorporating the processes indicated in Figure 1 and eq 1. Specifically, calculations are performed of the ground-state structures of singly doped $AlAr_N$ clusters for $N = 2-54$, of the dipole-allowed ultraviolet absorption cross sections of these clusters in Franck−Condon approximation over the spectral region of interest, and of the vibrational motions and fragmentation patterns following cluster ionization in the temperature range 10−30 K. Although significant advances have been made in theoretical treatments of the structures and properties of clusters of various types,[24] the complexities associated with spin−orbit coupling, anisotropic interactions, and the avoided crossing of the excited electronic potential energy surfaces in $AlAr_N$ clusters require special methods of treatment.

The required ground- and excited-state adiabatic electronic potential energy surfaces arising from these complex interactions are calculated employing ab initio procedures devised specifically for this purpose.[25] Absorption cross sections are obtained

from a classical Monte Carlo treatment of the vibrational degrees of freedom employing the calculated potential energy surfaces and the vertical oscillator strengths provided by the corresponding electronic transition moments.[26] As indicated above in connection with discussion of Figure 1, the shallow natures of the excited-state potential energy curves in AlAr obtained from the calculations relative to that of the Al^+Ar ion (see below) suggest that the 3p → 3d and 4p electronic excitation step will produce some degree of vibrational excitation in the neutral clusters but significantly less fragmentation than the ionization step. Specifically, the vibrational motions on the relatively shallow excited-state potential energy surfaces of the neutral clusters are sufficiently slow to ensure that ionization in the intense visible laser beam will take place well before significant cluster geometry changes can occur. By contrast, the strong gradients in the ionic potential energy surfaces and the significant differences in vertical and adiabatic ionization potentials give rise to considerable cluster-ion fragmentation on both short (nanosecond) and long (microsecond) time scales. These latter fragmentation patterns are obtained from quantum diffusion Monte Carlo calculations of initial vibrational states,[27] classical molecular dynamics simulations on the ionic potential energy surfaces,[26] and calculations of the residual cluster-ion energies remaining after finite (1 ns) propagation times to estimate the degree of additional Ar atom evaporation on a longer (microsecond) time scale. The essential aspects of these theoretical procedures are described immediately below, whereas complete descriptions of the methods are reported elsewhere.[25−27]

The adiabatic electronic potential energy surfaces of the neutral clusters are obtained from a multistep procedure that begins with multireference configuration-interaction (MRCI) calculations of all eight diatomic AlAr potential curves that correlate with the 3p, 4s, 3d, and 4p Al and $^1S_0$ Ar atomic limits employing a (17s,12p,5d,4f)/[7s,6p,4d,3f] atomic natural orbital basis set supplemented with four diffuse functions (1s,1p,1d,-1f). A state-averaged complete-active-space wave function with the three Al valence ($3s^23p$) electrons distributed in 13 orbitals is employed as a starting reference, employing the code suite MOLPRO to perform all calculations.[28] The diatomic potential curves, shifted to agree with the known Al energy values in the atomic separation limit,[29] are in very good but not precise accord (see below) with spectroscopic studies of the X(3p) $^2\Pi_{1/2}$ → B(4s) $^2\Sigma^+$, (3d) $^2\Delta$, (3d) $^2\Pi$, (3d) $^2\Sigma^+$, and (4p) $^2\Pi$ bands of the AlAr molecule.[19] The Ar−Ar ground-state potential energy curve is taken from previous calculations, which have been adjusted to account approximately for the nonadditive structural effects appropriate for simulation of Ar_N aggregates.[20]

The calculated diatomic potential curves are transformed into a 24-term atomic-product-like representation that allows construction of the many-body $AlAr_N$ cluster Hamiltonian matrix in the form of atomic and pairwise additive atomic-interaction matrices,[25]

$$\mathbf{H} = \mathbf{H}^{(\mathbf{Al})} + \sum_{\alpha=1}^{N}\{\mathbf{H}^{(\mathbf{Ar}_\alpha)} + \mathbf{V}^{(\mathbf{Al},\mathbf{Ar}_\alpha)}(\mathbf{R}_{\mathrm{AlAr}_\alpha}) + \sum_{\beta=1}^{N}(\beta>\alpha)\mathbf{V}^{(\mathbf{Ar}_\alpha,\mathbf{Ar}_\beta)}(\mathbf{R}_{\mathrm{Ar}_\alpha\mathrm{Ar}_\beta})\} \quad (2)$$

Here, the atomic energy matrix $\mathbf{H}^{(Al)}$ contains the known experimental Al energy levels on the diagonal,[29] as well as diagonal and off-diagonal terms that describe the Al spin−orbit interactions exactly in the atomic separation limit and provide estimates of the molecular splittings for finite separations in the absence of ab initio calculations.[30,31] The diagonal atomic matrices $\mathbf{H}^{(Ar_\alpha)}$ contain only the ground-state Ar atomic energy, whereas the diagonal pairwise Ar−Ar interaction matrices $\mathbf{V}^{(Ar_\alpha,Ar_\beta)}(\mathbf{R}_{Ar_\alpha Ar_\beta})$ are obtained from the aforementioned modified ground-state diatomic potential energy curve.[20] Finally, the Al−Ar interaction matrixes are obtained from the expression[25]

$$\mathbf{V}^{(\mathbf{Al},\mathbf{Ar})}(\mathbf{R}_{\mathrm{AlAr}}) = \mathbf{D}^{(\mathbf{Al},\mathbf{Ar})^\dagger}\cdot\mathbf{U}^{(\mathbf{Al},\mathbf{Ar})^\dagger}\cdot\mathbf{E}^{(\mathbf{Al},\mathbf{Ar})}\cdot\mathbf{U}^{(\mathbf{Al},\mathbf{Ar})}\cdot\mathbf{D}^{(\mathbf{Al},\mathbf{Ar})} - \mathbf{E}^{(\mathbf{Al},\mathbf{Ar})}(\infty) \quad (3)$$

where $\mathbf{E}^{(Al,Ar)}$ is the diagonal matrix of calculated AlAr potential curves, $\mathbf{D}^{(Al,Ar)}$ are appropriately ordered products ($\mathbf{D}^{(Al)} \otimes \mathbf{D}^{(Ar)}$) of Al and Ar atomic Wigner rotation matrices,[32] $\mathbf{U}^{(Al,Ar)}$ is the unitary transformation matrix connecting the diatomic basis with the atomic-product basis suitable for describing simultaneously multiple Al−Ar interactions in the cluster, and $\mathbf{E}^{(Al,Ar)}(\infty)$ is the asymptotic atomic-limit ($R_{AlAr} \rightarrow \infty$) value of the matrix of calculated diatomic potential energy curves $\mathbf{E}^{(Al,Ar)}$.

Nonadiabatic coupling matrix elements between the atomic-product states are also obtained from the unitary transformation matrix $\mathbf{U}^{(Al,Ar)}$ in the form[31]

$$\mathbf{P}^{(\mathbf{Al},\mathbf{Ar})}(\mathbf{R}_{\mathrm{AlAr}}) = -(\mathrm{d}\mathbf{U}^{(\mathbf{Al},\mathbf{Ar})}/\mathrm{d}R_{\mathrm{AlAr}})\cdot\mathbf{U}^{(\mathbf{Al},\mathbf{Ar})^\dagger} \quad (4)$$

where $\mathbf{U}^{(Al,Ar)}$ is generally constructed to ensure the equivalence of the invariant one-electron transition density matrix in the two representations.[25,33] In the case of the relatively weak dispersion interactions of interest here, however, it is judged sufficient to employ the matrix of dipole transition moments calculated in the two representations (diatomic and atomic-product) to construct the required transformation matrix, a procedure that corresponds to use of a dipole-operator-weighed integral over the transition density matrix in place of the more complicated transition density matrix itself. This approximation provides the simple expression $\mathbf{U}^{(Al,Ar)} = \mathbf{U}_d^{(Al,Ar)}\cdot\mathbf{U}_\infty^{(Al,Ar)^\dagger}$, where $\mathbf{U}_d^{(Al,Ar)}$ is the matrix that diagonalizes the molecular dipole transition moment matrix and $\mathbf{U}_\infty^{(Al,Ar)}$ diagonalizes its asymptotic ($R_{AlAr} \rightarrow \infty$) atomic-product limit. Note in this connection that some care must be exercised in employing phase- or sign-consistent electronic dipole transition moments in constructing the $\mathbf{U}_d^{(Al,Ar)}$ and $\mathbf{U}_\infty^{(Al,Ar)}$ matrices.[33]

Diagonalization of the many-body Hamiltonian matrix of eq 2 provides energy surfaces and eigenstates that include spin−orbit splittings and nonpairwise-additive anisotropic Al−Ar interactions and that incorporate the avoided crossings and other interactions required for a satisfactory representation of the excited electronic states of the clusters. Although the Ar atoms are formally assumed to remain in their ground $^1S_0$ state in this approach ($\mathbf{D}^{(Ar)} \rightarrow \mathbf{I}$), their charge distortions due to interactions with the Al and Ar atom are included in the diatomic and atomic-product states and are thereby incorporated in the calculated many-body cluster electronic states. The method is seen to be a logical extension to avoided crossing situations of previously described perturbative methods for employing atomic pair-interaction potentials in cluster and other aggregate calculations[34,35] and is an alternative computational implementation of a recently developed more general spectral theory of chemical interactions.[36,37]

Optical absorption cross sections are obtained from the calculated MRCI energies and dipole transition moments and classical Monte Carlo simulations of the vibrational motions on the calculated potential energy surfaces at 10−30 K.[26,33] The ground-state geometries of the clusters, which are employed only for visualization purposes, are provided by the lowest-

energy structure obtained from a sufficiently large configurational sampling space (~200 000 structures) for each cluster at 10 K. Although the calculations are performed at finite temperatures, it is found that there is little difference between the cluster structures so obtained and those derived from explicit energy minimization employing the system Hessian matrix in selected cases. Moreover, the thermally averaged cluster energies obtained from the former calculations include a semiclassical approximation to the effects of zero-point vibrational motions, and accordingly give estimates of the vibronic cluster energies (D_0) rather than electronic energies (D_e). Of course, there is ultimately no guarantee that the structures obtained from either Monte Carlo sampling or explicit energy minimization necessarily correspond to true global minima in view of the generally shallow natures of the cluster potential energy surfaces. Nevertheless, the calculated energies are expected to be very close to the true global-minimum energies, and the structures found should differ only slightly, if at all, from the global-minimum structures, particularly for the smaller clusters.

The degree of vibrational excitation and subsequent shake-off of Ar atoms from the ionized clusters associated with the dominant channel of Figure 1 is obtained from a two-step procedure involving kinematical and thermal phases of the fragmentation process. In the kinematical phase, an ensemble of initial $AlAr_N$ vibrational configurations, the vertical ionization energies of the neutral clusters, the zero-point equilibrium energies of the stable cluster-ions produced, and classical molecular dynamics (MD) simulations on the ionic surfaces are employed to estimate the nature and extent of prompt ($\leq$1 ns) cluster fragmentation. The calculations employ ionic potential energy surfaces based on the aforementioned accurate Ar−Ar potential and MRCI calculations of the $AlAr^+$ ground-state potential. In the thermal phase, the excess vibrational energies above the stable cluster-ion ground-state energies remaining in the cluster ions after completion of the kinematical phase (1 ns) of the fragmentation process are employed to estimate the additional degree of Ar atom thermal evaporation possible on a longer time scale (~30 μs). The short-time simulation provides insights into the dynamical mechanisms associated with formation of final stable cluster ions, in which the Al^+ ion is strongly solvated by Ar atoms (see below), whereas the results in the long-time limit provide the total degree of ionic cluster fragmentation possible in each case.

The parent ensemble of initial $AlAr_N$ vibrational configurations, obtained from diffusion quantum Monte Carlo studies described immediately below,[27] is vertically ionized to generate an ensemble of Al^+Ar_N configurations in the kinematical phase. These configurations are then propagated on the Al^+Ar_N potential surface for 50 000 molecular dynamics steps of 20 fs each for a 1 ns total simulation time. From images viewed every 0.1 ns, one or more Ar atoms are seen to be removed promptly from a cluster during the first half of the MD simulation, whereas ejection during the last half of the simulation occurs very infrequently. This transitional behavior signals the onset of the thermal phase of the fragmentation process. The parent ensemble of initial $AlAr_N$ vibrational configurations is obtained from a set of 200 diffusion quantum Monte Carlo (DQMC) simulations of the $AlAr_N$ cluster employing descendant tagging[38] to generate the quantum-mechanical ground-state probability distribution for a specific cluster size. Each DQMC simulation lasts for 1 ps of imaginary time and employs 500 replicas moving on the nonpairwise-additive potential surface defined by eqs 2 and 3. At the end of each DQMC simulation, the descendant tags of the initial replicas are compiled. These determine the weight that a particular starting configuration contributes to the quantum-mechanical probability distribution of the $AlAr_N$ structures and thus to the fragmentation pattern of the corresponding Al^+Ar_N ion. Each DQMC simulation typically contributes 10−15 sets of initial conditions to the MD simulation, so a total of 2000 to 3000 MD trajectories are computed.

The internal vibrational energies assigned to the ionic clusters in the aforementioned calculations follow from the parent ensemble of initial $AlAr_N$ cluster configurations, the known excess of energy deposited in the cluster following $1_{uv} + 1_{vis}$ photon absorption obtained from the difference between the vertical and adiabatic cluster ionization potentials, and the assumption that the passage from the intermediate excited state to the ionized state is sufficiently rapid to ensure that significant vibrational redistribution does not occur in the intermediate states (Figure 1). In this approximation, the initial ensemble of Al^+Ar_N configurations is generated by vertical ionization of the corresponding neutral $AlAr_N$ cluster and thus reflects the vertical projection of the zero-point motions of the atoms in the quantum mechanical ground state of the neutral cluster on the Al^+Ar_N potential surface, in which process the small kinetic energy of zero-point vibration in the ground state is neglected.

The fragmentation yield resulting from excitation and ionization of any initial cluster $AlAr_N$ is obtained in the thermal or long-time limit from the distribution of excess energies remaining in a particular cluster ion at the end (1 ns) of the kinematical phase of the simulation. This distribution accounts for the degree to which the earlier fragmenting Ar atoms lost during the kinematical phase remove the excess energy initially deposited in the cluster upon ionization, and the corresponding probability with which additional thermal evaporation is likely to occur in the statistical phase. That is, the difference between the vertical ionization energy of the cluster $AlAr_N$ and the ground-state equilibrium energy of the ionic clusters Al^+Ar_M ($M \leq N$) gives the maximum number of Ar atoms that can shake off from the cluster Al^+Ar_N at the outset, although this maximum need not be achieved because the promptly departing Ar atoms can remove more or less excess energy as dictated by the kinematical phase of the fragmentation process. It is assumed in the thermal phase that there are no long-lived metastable cluster ions trapped behind potential barriers, so all additional Ar evaporation that is energetically possible does, in fact, occur.

Finally, although the combined kinematical fragmentation/thermal evaporation process leads to the formation of a single specific final ionized cluster, Al^+Ar_M ($M \leq N$), for each trajectory, by employing a large ensemble of initial configurations, the probability distribution for a range of final cluster sizes M for an initial neutral cluster size N is computed. Accordingly, the fragmentation processes of neutral clusters $AlAr_N$ for the range of N values that contributes to formation of a specific cluster ion Al^+Ar_M are assembled in this way to provide the fragmentation coefficients $F_{NM}^{(+)}$ of eq 1, from which the theoretical spectrum appropriate for comparison with the measured cluster-ion action spectrum is obtained.

4. Results

In Figure 2 is shown a typical spectrum of Al^+Ar_M cluster ions recorded by time-of-flight $1_{uv} + 1_{vis}$ multiphoton ionization mass spectrometry employing $\lambda_{uv} = 315$ nm and $\lambda_{vis} = 630$ nm photons, obtained following the procedures described in sections 1 and 2. The areas under the individual peaks correspond to the expression of eq 1 for the indicated incident photon wavelengths and, accordingly, when properly normalized

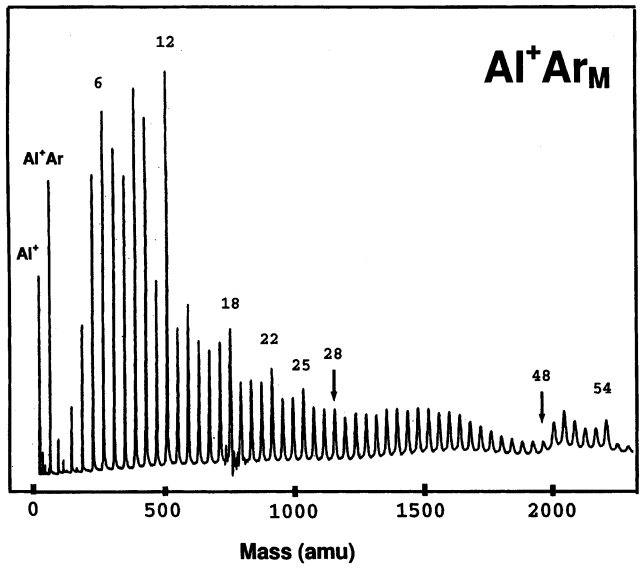

Figure 2. Typical experimental resonant $1_{uv} + 1_{vis}$ multiphoton ionization Al^+Ar_M mass spectrum obtained from $AlAr_N$ clusters employing $\lambda_{uv} = 315$ nm and $\lambda_{vis} = 630$ nm photons, as described in the text. Areas under the peaks provide the signals of eq 1 in the text. The M values of clusters ions thought to be particularly stable on the basis of icosahedral major and minor magic numbers are indicated.[39]

to the ultraviolet fluence, provide the left-hand side of the expression

$$N_M^{(+)}(h\nu_{uv}) \propto \sum_N P_N \sigma_{abs}^{(N)}(h\nu_{uv}) F_{NM}^{(+)} \qquad (5)$$

In eq 5, the ionization cross section and visible laser fluence have also been eliminated in light of the aforementioned saturation of the ionization step in the experiment. Consequently, the normalized data of Figure 2 correspond to the combination of the prior beam cluster-size distribution (P_N), the UV absorption cross sections of the neutral clusters [$\sigma_{abs}^{(N)}(h\nu_{uv})$], and the fragmentation coefficients of the ionic clusters ($F_{NM}^{(+)}$) indicated in eq 5. The widths of the peaks increase with the square root of the cluster-ion mass, potentially simplifying determination of the peak areas, although these are evaluated directly in the present work taking care to include the Jacobian that arises in the time-to-mass coordinate transformation. Mass peaks corresponding to Mackay icosahedral major ($M = 12$ and 54) and minor ($M = 18$, 22, 25, 28, and 48) magic-number structures are indicated in the figure for reference.[39] The results of Figure 2 are similar to but differ in detail from earlier ultraviolet photoionization mass-spectrometric measurements on $AlAr_N$ clusters that employ ArF and excimer-pumped dye lasers to study cluster-ion appearance potentials[10,11]

In Figure 3 are shown spectra recorded by detecting Al^+Ar_6 and Al^+Ar_{12} cluster ions as the incident ultraviolet photon wavelength is scanned over the Al 3p → 3d and 4p spectral range (~290−330 nm). The spectra shown are obtained from both resonant $1_{uv} + 1_{vis}$ and $2_{vis} + 1_{vis}$ multiphoton ionization. The laser dyes and dye mixtures employed provide a series of overlapping wavelength intervals in the ultraviolet from which the data sets of Figure 3 are derived. In most cases, ultraviolet-fluence-normalized spectral segments are matched by having scans overlap and scaling is achieved by equating the integral of the overlapped regions. In some cases, the signals in adjacent dye regions do not overlap, as is evident in Figure 3. In these cases, the relative scaling of the spectra is aided by matching slopes, when possible, and checking for consistency with the

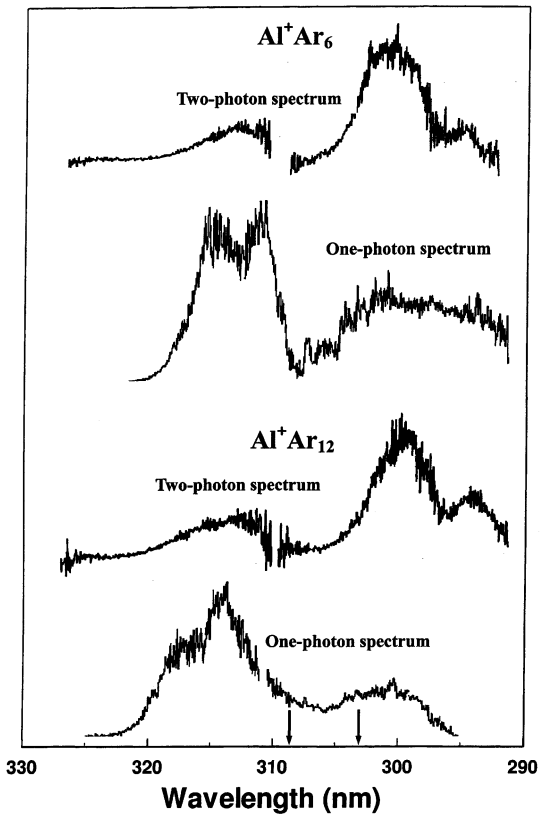

Figure 3. Experimental Al^+Ar_6 and Al^+Ar_{12} cluster-ion spectra obtained employing resonant $1_{uv} + 1_{vis}$ and $2_{vis} + 1_{vis}$ multiphoton ionization, separately normalized to the ultraviolet and visible laser fluence employed in each case, as functions of ultraviolet wavelength ($\lambda_{vis} = 2\lambda_{uv}$). The wavelengths of the 308 and 303 nm atomic Al 3p → 3d and 4p transitions (32 435.45 and 32 949 cm^{-1}, respectively)[29] are indicated by small vertical arrows. The origins of breaks in the recorded data are described in the text.

absolute magnitude of the fluence-normalized signals. These gaps lead primarily to uncertainty in the relative magnitudes of the red- and blue-shifted bands and not to uncertainty in the structure within the bands. The apparent fine structure in the data is noise resulting primarily from pulse-to-pulse variations in the laser fluence and in the pulsed cluster source.

Evidently, all four spectra in Figure 3 show structured bands to the red and to the blue of the 308 and 303 nm atomic Al 3p → 3d and 4p transitions, respectively. The appearance of these red-shifted bands is in marked contrast to the aforementioned Al matrix-isolation studies in rare gases, in which only blue-shifted bands are observed.[4−8] The two one-photon spectra evidently differ somewhat from each other in structural detail, whereas the two two-photon spectra exhibit some degree of similarity. Although both one- and two-photon excitation spectra show bands in similar wavelength regions, the one-photon bands are clearly relatively stronger to the red of the 308 nm line, whereas the two-photon bands are stronger to the blue of the 303 nm atomic Al line, in accordance with their presumptive 3p → 3d and 4p origins. The failure of the $2_{vis} + 1_{vis}$ spectra to scale as $\sim I_{vis}^3$ is judged to be a consequence of the aforementioned saturation of the final ionization step in the multiphoton process and not of saturation of the two-photon absorption step. Although theoretical interpretations of these two-photon data are possible, quantitative results are reported here only for the one-photon data sets of Figure 3, whereas qualitative remarks are made in connection with the two-photon spectra.

Multiphoton ionization spectra for other $AlAr_N$ clusters are generally similar to but different in detail from those shown in

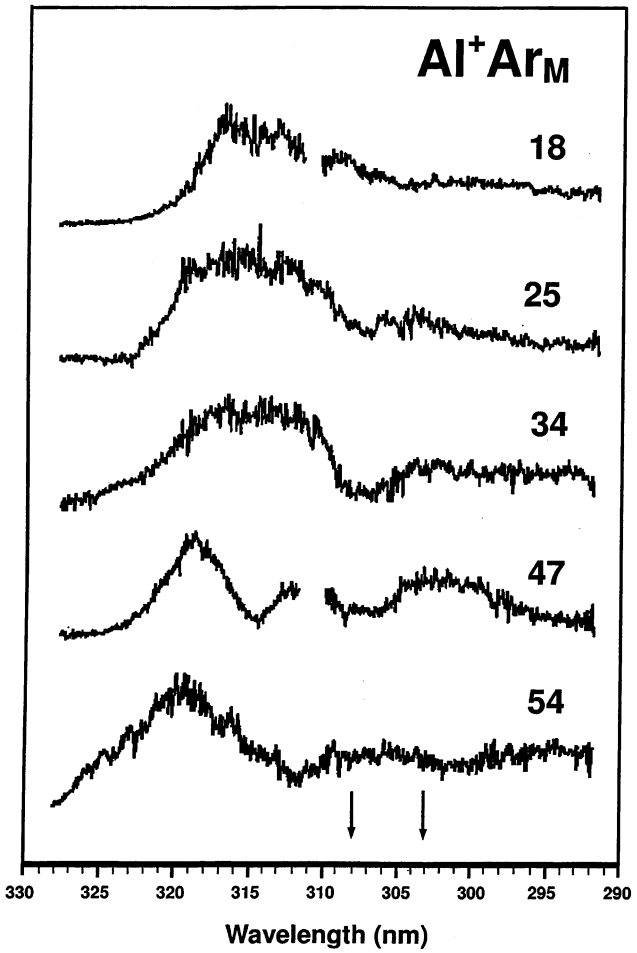

Figure 4. Experimental Al^+Ar_M cluster-ion spectra obtained employing resonant $1_{uv} + 1_{vis}$ multiphoton ionization, normalized to the ultraviolet laser fluence employed in each case, as functions of ultraviolet wavelength ($\lambda_{vis} = 2\lambda_{uv}$). The wavelengths of the 308 and 303 nm atomic Al 3p → 3d and 4p transitions (32 435.45 and 32 949 cm^{-1}, respectively)[29] are indicated by small vertical arrows. The origins of breaks in the recorded data are described in the text.

Figure 3.[15,22] Figure 4 provides an overview of the peaks and widths of the broad red- and blue-shifted asymmetric bands that appear in one-photon excitation ($1_{uv} + 1_{vis}$) data sets recorded for selected clusters in the range $M = 18-54$. The degree of red band shift is seen to increase very gradually with cluster size, with a distinct steplike behavior evident in the red shifts for $M = 47$ and 54, possibly associated with icosahedral shell or subshell closings. The broad blue-shifted bands are seen to be only weakly structured, although there is some hint of peaks evident for $M = 47$ and possibly 54. These blue shifts are not in accord with the results of matrix-isolation studies, which show strong distinct Al bands in Ar matrixes at 291 and 286 nm.[4-7] Comparison of Figures 3 and 4 suggests the presence of double peaks in the red-shifted bands for $M = 6$, 12, and 47, which are not apparent in the other spectra.

In Figures 5 and 6 are shown calculated ground- and excited-state potential energy curves for molecular AlAr states correlating with the 3p, 3d, and 4p atomic Al limits and the Ar $^1S_0$ ground state, as well as the ground-state potential curve of Al^+-Ar. Figure 5 employs an energy scale that provides an overview of the entire diatomic excitation and ionization spectrum, whereas Figure 6 provides more detailed information. Evidently, the 3d and 4p manifolds of diatomic states are nearly degenerate on the scale of Figure 5, suggesting that the associated excited electronic states of the clusters obtained from eqs 2 and 3 will

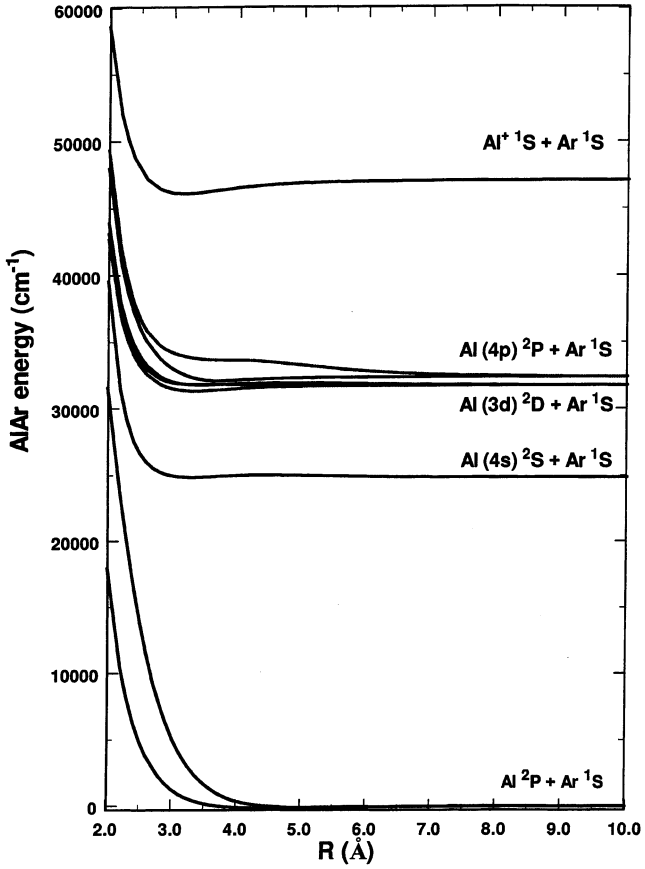

Figure 5. Calculated diatomic AlAr and Al^+Ar potential energy curves obtained from multireference configuration-interaction methods indicated in the text, shifted to agree with the experimentally known atomic and ionic Al energy levels.[29] The ground-state energies of the ($^2P_{1/2}$)Al and ($^1S_0$)Ar atoms are arbitrarily set to zero.

generally be complex mixtures of these contributions. By contrast, cluster states arising from the 4s potential curve of Figure 5 are expected to be less complex and to give rise to less structured spectra.[11]

The calculated ground-state X $^1\Sigma^+$ $AlAr^+$ molecular ion potential curve ($D_e \approx 1000$ cm^{-1}) shown in Figure 5 is in good accord with experimental values ($D_e = 982.3$ cm^{-1})[19] and is seen to provide an order of magnitude greater binding than that of the ground $^2\Pi_{1/2}$ state of the neutral molecule ($D_e \approx 100$ cm^{-1}) shown in Figure 6a. The calculated ionic curve also has a significantly smaller equilibrium interatomic separation (~3.1 Å) than the calculated neutral curve (~4.0 Å). These large differences have implications for the role of cluster-ion fragmentation in accounting for the measured data, as is discussed in detail below. All potential energy curves in Figures 5 and 6 have been uniformly shifted in energy to provide agreement with the known experimental atomic or ionic separation limits,[29] employing a convention in which the ground-state atomic ($^2P_{1/2}$)Al and ($^1S_0$)Ar energies are arbitrarily set to zero. This ad hoc procedure facilitates comparisons with the spectral data and ensures that the resulting curves are in good agreement with the reported spectral measurements in AlAr.[19,22,23] The calculations, however, uniformly underestimate the excited-state AlAr binding energies (D_0) of the 3d and 4p states with values obtained for the 0−0 (3p) X $^2\Pi_{1/2}$ → (3d) $^2\Delta$, (3d) $^2\Pi$, (3d) $^2\Sigma$ transitions consequently falling ~0.5% to the blue of the reported experimental values and the 0−0 (3p) X $^2\Pi_{1/2}$ → (4p) $^2\Pi$ transition falling ~1.5% to the blue of the experimental value.[19,23] Although these discrepancies are relatively small in absolute value (~200−400 cm^{-1}), they have discernible effects

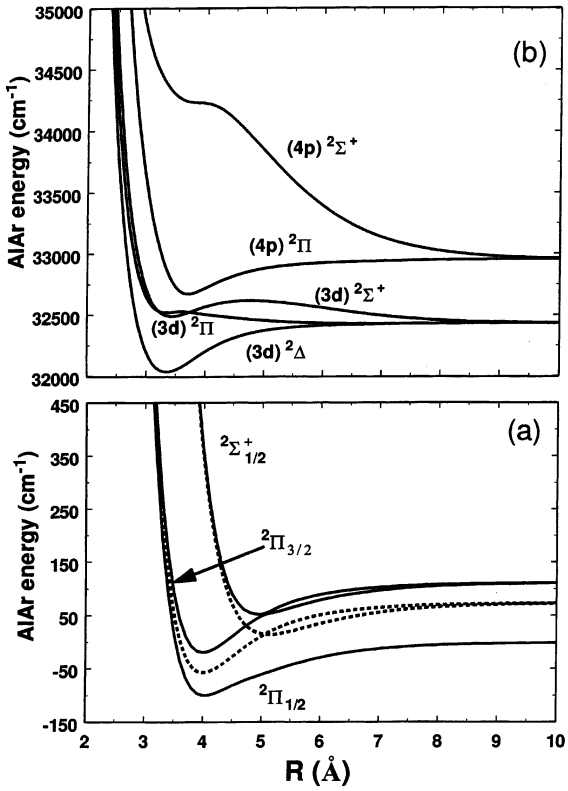

Figure 6. Calculated diatomic AlAr potential energy curves obtained as in Figure 5 and as discussed in the text: (a) ground-state $^2\Pi_{1/2}$, $^2\Pi_{3/2}$, and $^2\Sigma^+_{1/2}$ spin−orbit split curves (—) arising from the $^2\Pi$ and $^2\Sigma^+$ curves (− − −) of Figure 5; (b) excited-state 3d and 4p AlAr potential energy curves. All curves have been shifted vertically to dissociate to the known atomic energy separation limits.[29]

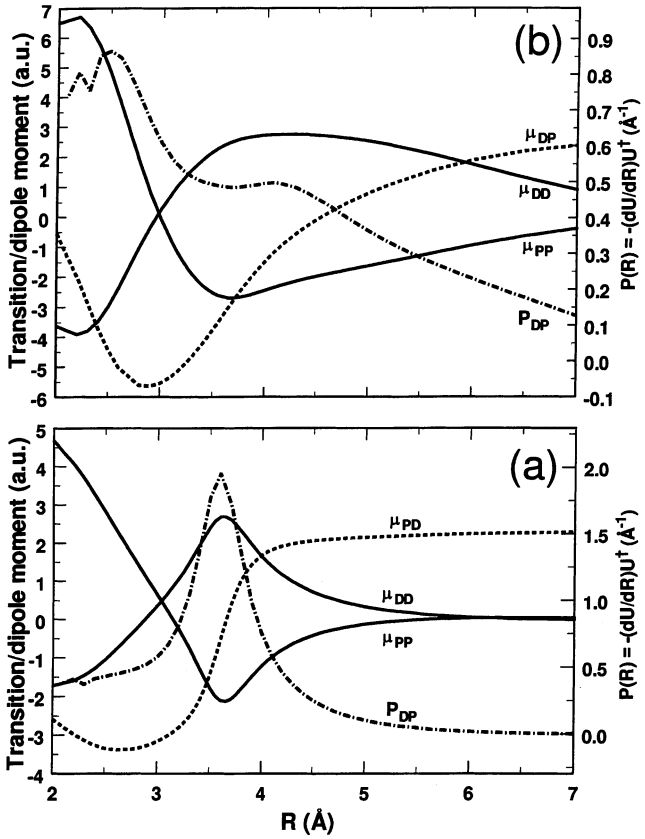

Figure 7. Calculated diatomic AlAr dipole moments and transition moments corresponding to the potential energy curves of Figures 5 and 6: (a) dipole moments for D ≡ (3d) $^2\Pi$ and P ≡ (4p) $^2\Pi$ states (—), transition moment (− − −), and interaction matrix element (− · −) of eq 4; (b) dipole moments for D ≡ (3d) $^2\Sigma$ and P ≡ (4p) $^2\Sigma$ states (—), transition moment (− − −), and interaction matrix element (− · −) of eq 4.

on the placement of strong features in the calculated cluster absorption cross sections.

Spin−orbit splitting effects have been included in the ground-state potential (solid line) shown in Figure 6a, constructed from eqs 2 and 3 using the calculated (3p) $^2\Sigma^+$ and (3p) $^2\Pi$ curves (dashed lines) and the experimental $^2P_{1/2}-^2P_{3/2}$ atomic Al splitting (112 cm^{-1}).[29] The binding energy of the calculated ground-state (3p) X $^2\Pi_{1/2}$ potential ($D_e \approx 100$ cm^{-1}) underestimates the current experimental value ($D_e = 122.4$ cm^{-1}),[19] although this small discrepancy (∼22 cm^{-1}) has little effect on the cluster structures and the absolute values of the calculated transition energies. The resulting spin−orbit $^2\Pi_{1/2}-^2\Pi_{3/2}$ splitting at the equilibrium interatomic separation is in excellent accord with independently obtained theoretical values.[40] The repulsive nature of the (3p) $^2\Sigma^+_{1/2}$ potential curve of Figure 6a has significant implications for the predicted geometries of the ground-state clusters, although it lies ∼450 cm^{-1} above the ground-state AlAr potential minimum at $R_e \approx 4$ Å.

The (3d) $^2\Pi$, (4p) $^2\Pi$, and (3d) $^2\Sigma^+$, (4p) $^2\Sigma^+$ curves shown in Figure 6b evidently undergo avoided crossings in the vicinity of the vertical electronic or Franck−Condon zone ($R \approx 4$ Å) of the ground-state curve. These interactions are also evident in Figure 7, which reports corresponding calculated electronic dipole moments and transition moments connecting the two pairs of interacting diatomic states. The two avoided-crossing interactions are also indicated in Figure 7 by the dot−dashed curves giving the nonadiabatic coupling matrix elements of eq 4 obtained from the unitary transformation connecting the adiabatic and atomic-product states.[25,33] In fact, the (3d) $^2\Sigma^+$ and (4p) $^2\Sigma^+$ curves evidently undergo two distinct avoided-crossing and recrossing interactions, as revealed by the variation of the associated moments and interaction matrix elements in Figure 7. The repulsive or attractive behaviors of the excited-state potential curves and moments of Figures 6 and 7 can be understood qualitatively on the basis of the spatial characteristics of the atomic Al 3d and 4p orbitals contributing to the individual molecular states, which allow closer approach in Π configurations than in Σ configurations. Note also that the diffuse 3d and 4p Al orbitals are significantly penetrated by the smaller Ar atom, accounting for the similarity of the repulsive walls of the excited-state potential curves of Figures 5 and 6b to that of the Al^+Ar ground molecular ionic state shown in Figure 5. The interactions of Figure 7 provide the largest off-diagonal elements in the excited-state portion of the $\mathbf{U}^{(Al,Ar)}$ matrix of eqs 3 and 4, whereas the spin−orbit and Σ−Π interactions provide off-diagonal terms in the ground-state portion of the Hamiltonian matrix. The latter terms arise from the Wigner rotation matrices in eq 3, which accomplish the geometrical portion of the transformation from diatomic to atomic-product states,[32] generally providing off-diagonal terms in all cases in the atomic-product representation.

The potential energy curves and dipole moments of Figures 5−7 and the transformation matrix $\mathbf{U}^{(Al,Ar)}$ obtained from the moments provide the necessary and sufficient information required to construct the Hamiltonian matrix of eqs 2 and 3 and to implement the theoretical development of section 3. In Figure 8 are shown the predicted ground-state geometries of selected small ($N = 3-5$) clusters and cluster ions obtained from Monte Carlo sampling at 10 K. The structures of the three neutral clusters shown (distorted C_{3v}, C_{2v}, C_{2v}) are largely the

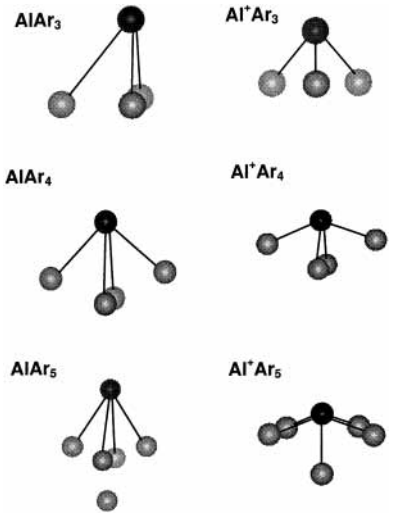

Figure 8. Calculated equilibrium geometries of $AlAr_N$ and Al^+Ar_N clusters obtained from classical Monte Carlo sampling at 10 K, as discussed in the text. See also Figures 9 and 10.

consequence of the competition between the anisotropic Al−Ar interaction and the isotropic Ar−Ar interaction, which are of comparable strength. There is no evidence in Figure 8 of the planar structures found in previous related studies of small (3^2P)-$NaAr_N$ clusters.[41] In this latter case, the large excited-state (3^2P)-Na−Ar $^2\Pi$ binding energy ($\sim$600 cm^{-1}) presumably overcomes competition with the smaller Ar−Ar attraction found to be important in the present study. Similar planar configurations have been suggested as appropriate in $AlHe_N$ clusters,[12] although definitive theoretical studies are apparently not available in these cases. Studies of BAr_N clusters employing potential energy surfaces obtained from methods closely related to the present study but in the absence of spin−orbit interactions apparently also report external-site metal atom locations in all cases considered.[18]

The fourth Ar atom in $AlAr_4$ in Figure 8 apparently coordinates with both Al and the three Ar atoms in $AlAr_3$ to form a C_{2v} structure, whereas the fifth Ar atom in $AlAr_5$ coordinates with four Ar atoms rather than with the Al radical. By contrast, the previously reported BAr_N study predicts a distorted BAr_5 octahedron, with the B atom in a site having five nearest neighbors.[18] This difference is possibly related to the more important role spin−orbit splitting in Al (112 cm^{-1}) plays in the $AlAr_N$ cluster structures relative to that of atomic B (16 cm^{-1})[29] in the BAr_N clusters. Specifically, the diatomic $^2\Pi_{1/2}$, $^2\Pi_{3/2}$, and $^2\Sigma^+_{1/2}$ AlAr states are spin−orbit-split mixtures of the $^2\Pi$ and $^2\Sigma^+$ states, resulting in more complex angular dependences in the ground states of the $AlAr_N$ clusters than in the absence of this mixing. The ionic structures of Figure 8 (C_{3v}, C_{2v}, C_{2v}) are qualitatively similar to corresponding Ar_N clusters, with $AlAr_5^+$ exhibiting the characteristics of a fragment of an icosahedral arrangement. Although the neutral and ionic structures of Figure 8 are similar for $N = 3$ and 4, the different $N = 5$ structures reflect the significantly different interactions of Al and Al^+ atoms with solvating Ar atoms. The Ar atoms evidently coordinate in Figure 8 with Al^+ at the diatomic Al^+-Ar equilibrium distance (Figure 5) with the Ar atom positions arranged in a manner to minimize the cluster energy through Ar−Ar attractions at these fixed Al^+−Ar distances.

The $AlAr_N$ cluster structures and related attributes reported here are independently verified by employing a second set of $^2\Pi$ and $^2\Sigma^+$ ground-state potential energy curves obtained from so-called coupled-cluster CCSD(T) calculations.[42] In contrast

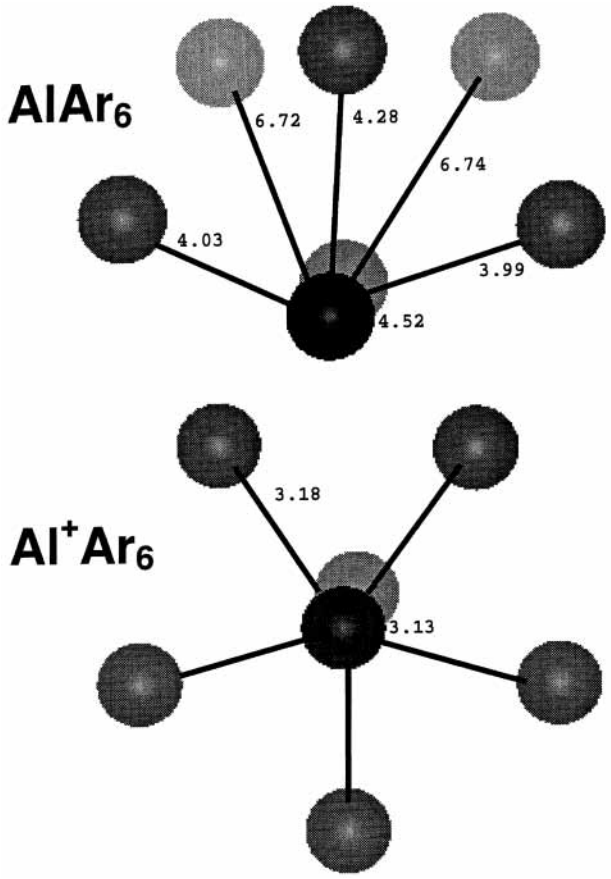

Figure 9. Calculated equilibrium geometries of icosahedral-like $AlAr_6$ and Al^+Ar_6 clusters obtained from classical Monte Carlo sampling at 10 K, as discussed in the text. Nearest- and next-nearest-neighbor Al−Ar and Al^+−Ar distances (Å) are indicated to help define quantitatively the geometries of the clusters.

to the MRCI calculations, which provide an orthogonal set of eigenfunctions appropriate for both ground and excited states, the CCSD(T) calculations concentrate on the ground-state $^2\Pi$ and $^2\Sigma^+$ curves only, providing a highly accurate ground-state $^2\Pi_{1/2}$ potential energy curve ($D_e = 127.7$ cm^{-1}, $R_e = 3.90$ Å) in excellent accord with experimental values ($D_e = 122.4$ cm^{-1}, $R_e = 3.79$ Å).[19] No significant differences are found between the structures obtained from the CCSD(T) potential energy curves and those of Figure 8.

Figures 9 and 10 depict the structures of $AlAr_6$ and $AlAr_{12}$ clusters, respectively, and their corresponding ions determined by Monte Carlo sampling at 10 K. The $AlAr_6$ cluster of Figure 9 has a structure highly similar to the slightly distorted icosahedral $AlAr_{12}$ cluster of Figure 10 with the neutral Al atom appearing in an external cap-site location. The former structure evidently derives from the latter by removal of two Ar atoms from the nearest-neighbor shell and four Ar atoms from the next-nearest-neighbor shell in $AlAr_{12}$. It is found that the Al atom prefers an external or surface location in the ground states of all of the larger neutral clusters studied ($5 \le N \le 54$), although structures other than the cap-site arrangement of Figures 9 and 10 appear, including ones in which the Al atom appears in a pocket site on the surface of largely icosahedral Ar_N structures. This complexity of structures arises from the aforementioned competition between the similarly attractive isotropic Ar−Ar and anisotropic Al−Ar ground-state potentials ($D_0 \approx 100$ cm^{-1} in each case) and the repulsive nature of the Al−Ar interaction in the $^2\Sigma^+_{1/2}$ arrangement of Figure 6a.

In contrast to the neutral structures, the Al^+ ion in Al^+Ar_{12}

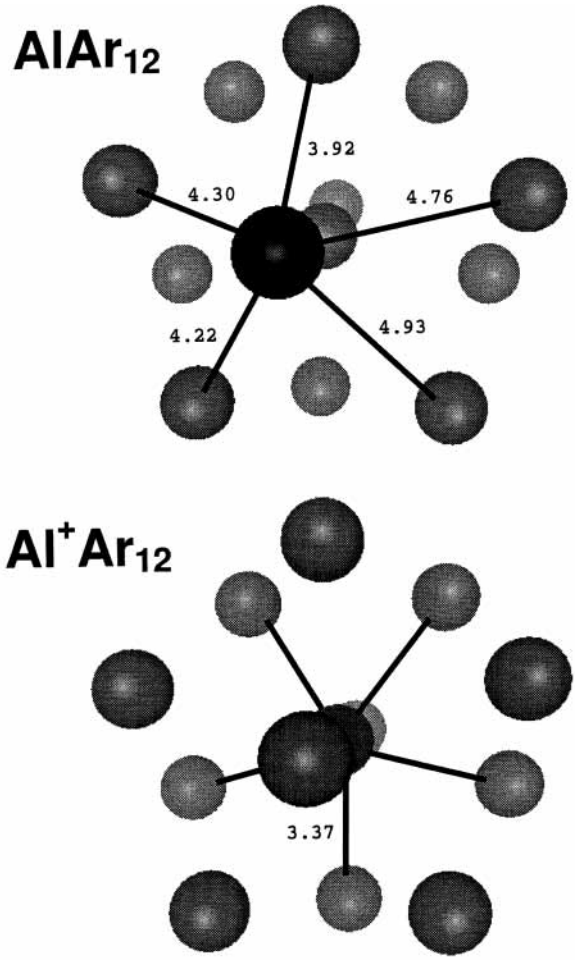

Figure 10. Calculated equilibrium geometries of icosahedral $AlAr_{12}$ and Al^+Ar_{12} clusters obtained from classical Monte Carlo sampling at 10 K, as discussed in the text. Nearest-neighbor Al−Ar and Al^+−Ar distances (Å) are indicated to help define quantitatively the geometries of the clusters.

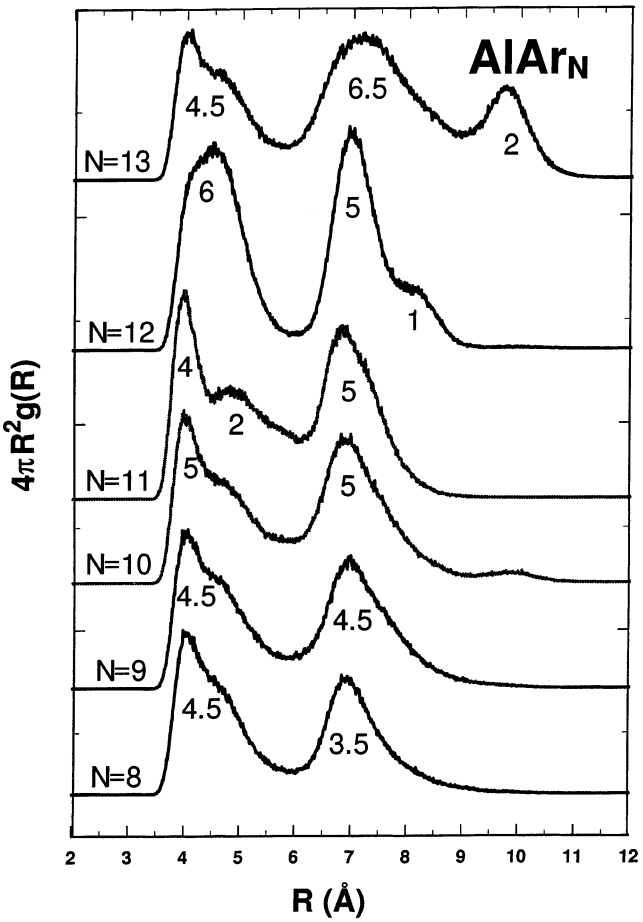

Figure 11. Radial distribution functions (Al−Ar) for $AlAr_N$ clusters ($N = 8-13$) obtained from classical Monte Carlo calculations at $T =$ 30 K and the many-body potential energy surfaces of the Hamiltonian matrix of eqs 2 and 3, as discussed in the text. Also shown are the approximate numbers of Ar atoms in the shells of the radial distributions functions relative to the Al position.

ion of Figure 10 is seen to be completely surrounded by Ar atoms and to form a perfect icosahedron, whereas the Al^+Ar_6 ion of Figure 9 evidently derives from the former by removing six nearest-neighbor Ar atoms from one side of the structure. Evidently, the Al^+Ar_6 ion does not form a highly symmetrical O_h structure in its ground state because of Ar−Ar attraction, which, although an order of magnitude weaker than the Al^+−Ar interaction, serves to lower the energy in the structure of Figure 9 relative to that of the symmetric O_h structure. Although a comprehensive discussion of the structures of all of the clusters studied is beyond the interests of the present report, qualitative structural comments are made below in selected cases of particular interest.

In Figures 11 and 12 are shown calculated Al−Ar radial distribution functions for selected $AlAr_N$ clusters ($N = 8-13$ and 23−28), obtained at 30 K following the development of section 3. For the smaller clusters of Figure 11 ($8 \le N \le 13$), the Al atom assumes a cap-site location on distorted icosahedral-like Ar_N arrangements in all cases. The fractional numbers of atoms in the radial shells for $N = 8$, 9, and 13 are due to thermal broadening at 30 K, which merges the first two radial shells and makes asssignments of Ar atoms to these somewhat arbitrary, rather than to transitions between structural isomers in these cases. The corresponding lower-temperature (10 K) radial distribution functions (not shown) reveal only integer numbers of Ar atoms in substantially narrower, more-distinct shells in these cases. For $N = 8$ and 9, the structures are similar to that of Figure 9 for Al^+Ar_6 but with additional Ar atoms appearing in nearest- and next-nearest-neighbor shells. The $N = 11$ cluster exhibits a remarkable structure at 10 K in which the 11 Ar atoms are arranged in a classical icosahedral form but with two atoms missing on one side, where the Al atom coordinates with three planar Ar nearest neighbors. This unique arrangement evidently allows the three planar Ar atoms to minimize the $^2\Sigma^+_{1/2}$ component present in the manifold of potential curves that contribute to the ground-state structure. The reduction in nearest-neighbor Ar atoms in this particular cluster is also evident from the radial distribution function of Figure 11, which shows a sharp peak in the first shell even at 30 K. By contrast, for $N = 13$ the stable structure is that of an Ar_{13} icosahedron with the external Al in a pocket site coordinated symmetrically with three Ar atoms. The Al atom in this structure can migrate at 30 K from one equivalent pocket site to another, although each of these isomers gives rise to the same radial distribution function.

The fractional coordination numbers in the larger clusters of Figure 12 are of somewhat more complex origin, involving both thermal broadening and access to more significant structural changes at 30 K relative to the situation for smaller clusters. In the cases of $N = 24$ and 25, for example, the stable structures at 10 K show the Al atom in cap-site-like locations coordinated with *seven* Ar atoms in globally icosahedral symmetries that are broken by the presence of the additional nearest-neighbor Ar atom. These low-energy configurations contribute only

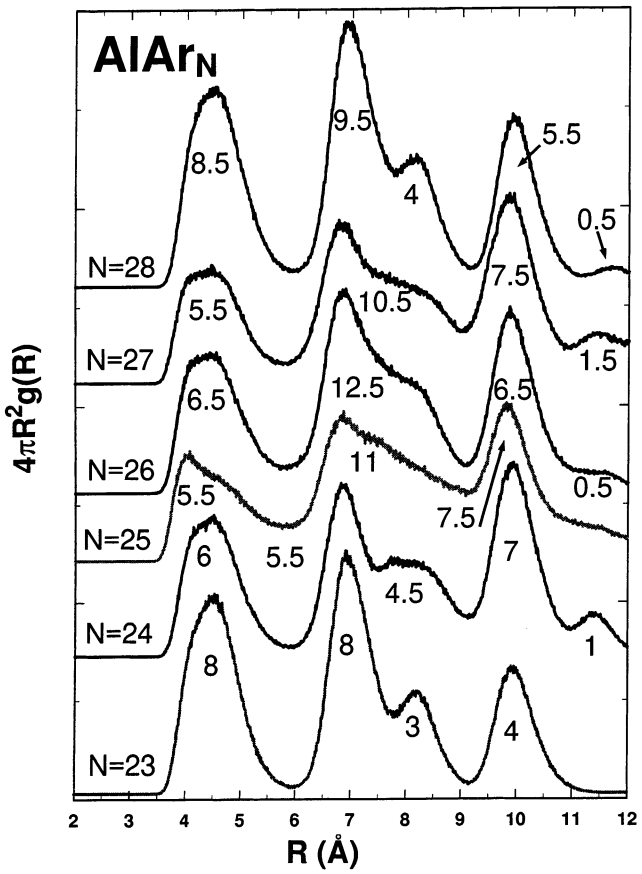

Figure 12. Radial distribution functions (Al−Ar) for $AlAr_N$ clusters ($N = 23-28$) obtained from classical Monte Carlo calculations at $T =$ 30 K and the many-body potential energy surfaces of the Hamiltonian matrix of eqs 2 and 3, as discussed in the text. Also shown are the approximate numbers of Ar atoms in the shells of the radial distributions functions relative to the Al position.

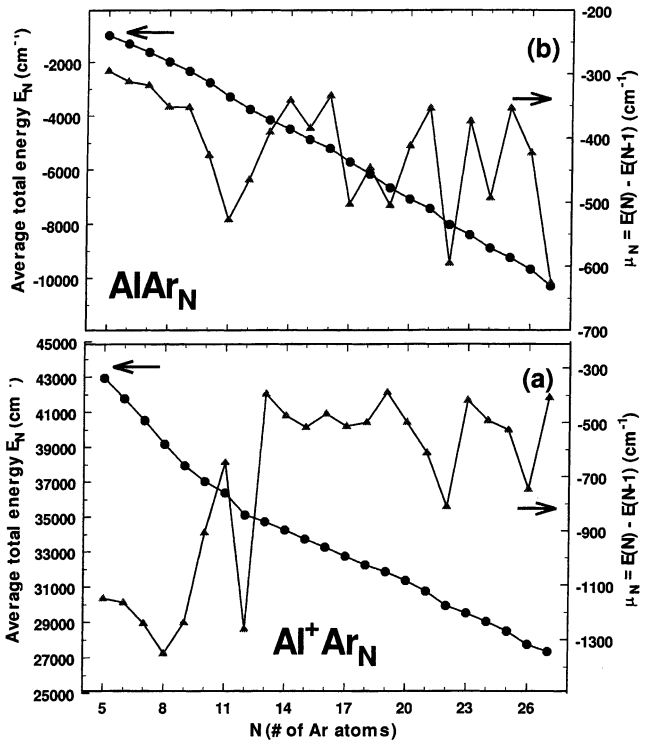

Figure 13. Ground-state vibronic binding energies of (a) Al^+Ar_N and (b) $AlAr_N$ clusters calculated at 30 K employing the interaction potentials of Figures 5 and 6 and the Hamiltonian of eqs 2 and 3, as discussed in the text. The associated "chemical potentials" are obtained from the differences $\mu_N = E_N - E_{N-1}$.

weakly to the higher-temperature radial distribution functions, however, with the "extra" nearest-neighbor Ar atoms withdrawing to the far side of the cluster at higher temperatures in most of the structures sampled. This thermal behavior accounts for the approximately six Ar nearest-neighbor atoms in the $N =$ 24 and 25 distributions of Figure 12. Although each cluster is an individual molecule with a unique ground-state geometry at low temperature, thermal effects can play a significant role in the apparent structures and other physical attributes of the clusters at moderately elevated temperature. It should be noted that the calculated spin−orbit excited potential surfaces of the clusters derived from the potential energy curves of Figure 6a are found to be at least 150 cm^{-1} vertically above the ground-state energy surfaces at the equilibrium geometries in all cases so do not contribute to the cluster structures and radial distribution functions of Figures 8−12 at the temperatures considered (10−30 K).

Additional aspects of the ground-state structures and energies of the neutral and ionic clusters are reported in Figure 13, which gives total cluster and cluster-ion energies and corresponding "chemical potentials" [$\mu(N) = E(N) - E(N-1)$]. Evidently, the calculations for the Al^+Ar_N clusters suggest an extra stability characteristic of magic-number icosahedra ($N = 12$ and 22), in accordance with the isotropic interactions in operation and the results of Figures 8−10 in these cases. Although the ionic energies are constructed from pairwise-additive potentials, the Ar−Ar potential employed has been modified to account approximately for nonadditive effects in bulk Ar,[20] and the strong Al^+−Ar interaction potential of Figure 5 includes the major effects of pairwise polarization important in ionic clusters with only smaller many-body self-consistent effects neglected. In contrast to the cluster ions, the results for the $AlAr_N$ clusters suggest greater stability at $N = 11$. This circumstance is related to the aforementioned more complex nature of the ground-state potential energy surfaces in operation in the neutral clusters arising from the anisotropic and spin−orbit split Al−Ar interaction potentials of Figure 6a. The stable $N = 22$ cluster reveals a cap-site location for the Al atom on an icosaheral Ar atom arrangement, giving rise to a radial distribution function in which there are six nearest-neighbor Ar atoms (not shown).

In Table 1 are shown calculated vertical and adiabatic ionization potentials of the neutral clusters $AlAr_N$ for $N = 1-30$ obtained from the development of section 3 at 30 K, in comparison with previously reported experimental appearance potentials.[10,11] The adiabatic values shown are obtained from the differences of the calculated total ground-state vibronic energies of the neutral and ionic clusters at their individual equilibrium geometries, whereas the vertical ionization potentials entail evaluation of the total Al^+Ar_N energies at the ground-state equilibrium geometries of the corresponding neutral clusters. Evidently, the measured appearance potentials, which are estimated from a figure provided in the experimental report,[10,11] fall between the calculated adiabatic and vertical ionization potentials in each case. The measured values clearly favor the calculated vertical ionization potentials, except for the very smallest clusters. These measured potentials are obtained following a procedure that attempts to minimize the effects of Ar atom shake off following cluster ionization by systematically lowering the ultraviolet laser photon energy employed to identify the threshold energy for the appearance of specific cluster ions. In light of the significant differences in neutral and ionic cluster geometries predicted here (Figures 8 and 9), however, the Franck−Condon factors for adiabatic ionization are expected

TABLE 1: Theoretical and Experimental Ionization Potentials of $AlAr_N$ Clusters[a]

N	vert[b]	exptl[c]	adiab[d]	*N*	vert[b]	exptl[c]	adiab[d]
1	5.93	5.88	5.88	16	5.78	5.64	4.77
2	5.88	5.81	5.78	17	5.74	5.63	4.76
3	5.86	5.75	5.55	18	5.74	5.63	4.78
4	5.86	5.73	5.45	19	5.73	5.63	4.77
5	5.82	5.72	5.34	20	5.69	5.62	4.77
6	5.80	5.71	5.23	21	5.71	5.61	4.74
7	5.86	5.71	5.11	22	5.74	5.59	4.69
8	5.80	5.70	4.99	23	5.65	5.59	4.71
9	5.90	5.69	4.93	24	5.73	5.57	4.70
10	5.74	5.67	4.92	25	5.71	5.55	4.67
11	5.74	5.67	4.82	26	5.68	5.53	4.64
12	5.74	5.67	4.82	27	5.73	≤5.5	4.67
13	5.81	5.65	4.80	28	5.60	≤5.5	4.64
14	5.80	5.64	4.79	29	5.71	≤5.5	4.64
15	5.76	5.64	4.77	30	5.67	≤5.5	4.64

[a] Values in eV obtained as indicated and discussed in the text. The atomic Al ionization potential is 5.984 eV.[29] [b] Vertical ionization potentials obtained from the theoretical development of section 3. [c] Experimental potentials for the appearance of cluster ions Al^+Ar_N.[10,11] [d] Adiabatic ionization potentials obtained from the theoretical development of section 3.

TABLE 2: Calculated Al^+Ar_N Cluster-Ion Fragmentation Coefficients[a,b]

	M							
N	5	6	7	8	9	10	11	12
8	0.838	0.157						
9	0.522	0.475	0.002					
10	0.013	0.852	0.136					
11		0.211	0.774	0.015				
12			0.192	0.794	0.014			
13		0.008	0.847	0.145				
14			0.204	0.756	0.040			
15			0.017	0.789	0.194			
16			0.017	0.528	0.453	0.002		
17				0.040	0.889	0.067	0.004	
18					0.139	0.752	0.087	0.022
19					0.423	0.542	0.030	0.001
20					0.074	0.786	0.131	0.008
21					0.003	0.283	0.446	0.264
22						0.011	0.148	0.772
23						0.021	0.151	0.797
24								0.657
25								0.107
26								0.040
27								0.002

[a] Fragmentation coefficients $F_{NM}^{(+)}$ of eqs 1 and 5 for production of cluster ions Al^+Ar_M from vibrationally excited parent ions Al^+Ar_N at 30 K, obtained following the theoretical development of section 3. The values shown, which are normalized to unity when summed over *M* for fixed *N*, include only the kinematical phase (≤1 ns) of the fragmentation process described in the text. [b] Entries not reported are judged too small ($<10^{-3}$) to contribute measureably to the fragmentation process.

to be vanishingly small. Accordingly, on the basis of the present calculations, the reported appearance potentials refer to thresholds for vertical ionization rather than adiabatic ionization, in accord with the results of Table 1.

To clarify further the effects of cluster-ion fragmentation quantitatively in connection with the results of Table 1, Table 2 reports calculated shake-off coefficients, $F_{MN}^{(+)}$, for production of cluster ions Al^+Ar_M from vibrationally excited ions Al^+Ar_N ($N > M$), obtained following the development of section 3. The values shown are normalized to unity when summed over *M* for a given *N* value. In each case, the excited ions Al^+Ar_N start out with excess internal energies given by the differences between the vertical and adiabatic ionization potentials of Table 1. The fragmentation patterns reported in Table 2 refer to prompt events only, occurring during the 1 ns kinematical phase. Accordingly, the ions so produced generally still retain excess internal energy, which can drive additional Ar atom evaporation during the thermal phase of the fragmentation process. The results of Table 2 suggest that there will be significant prompt fragmentation in all clusters considered when vertical ionization is energetically possible and that no parent ions will remain under these conditions. Evidently, relatively small bands of two or three ions are produced by fragmentation of each parent cluster ion, whereas larger bands of 5−10 parent ions can contribute to the production of a given fragment ion.

On the foregoing basis, in which the experimental appearance potentials of Table 1 are thought to correspond to measurements performed in the threshold energy region of the vertical ionization process, fragmentation of parent ions is judged complete, and only fragment ions should be detected. In the case of $N = 12$, for example, the measured appearance potential (5.67 eV) of Table 1 is sufficient to ionize those neutral clusters ($N \approx 23-29$) that fragment to produce significant amounts of Al^+Ar_{12} ions, according to the results of Table 2. Similarly, for $N = 6$, the measured ionization potential (5.71 eV) can produce Al^+Ar_6 ions by fragmentation of $N \approx 10-13$ neutral clusters, and similar remarks apply in other cases, as well. The nature of the kinematical fragmentation process, revealed by images viewed every 0.1 ns, shows a sudden collapse of the nearest-neighbor Ar atom shell toward Al^+ upon ionization in all cases and a subsequent outward radial rebound of this shell, resulting in ejection of the outermost Ar atoms by knock-on collisions. Although these observations are highly suggestive, more detailed fragmentation calculations, employing sub-vertical-threshold initial internal energies, quantum methods to probe these threshold energy regions, and an expression similar to eq 1 to include simultaneous contributions from a range of neutral clusters, are required to make unambiguous quantitative predictions and interpretations of the experimental appearance potentials.[10,11]

Although interest centers here on quantitative interpretations of the measured action spectra, it is useful to first note that the diatomic results of Figures 5−7 provide the basis for qualitative interpretations of the spectral data of Figures 3 and 4. Specifically, the intensity distributions of the one- and two-photon excitation spectra of Figure 3 are in good qualitative accord with the calculated AlAr potential energy curves of Figure 6b and with the associated dipole transition moments of Figure 7. The potential curves indicate that the (3d) $^2\Delta$ state remains furthest to the red of the atomic Al 3d state, whereas the (4p) $^2\Pi$ state appears furthest to the blue of the atomic 4p state for all interatomic distances with the dipole intensity of the nominally forbidden X (3p) $^2\Pi_{1/2} \rightarrow$ (4p) $^2\Pi$ transition attributed to 3d/4p mixing associated with the avoided crossing of the (3d) $^2\Pi$ and (4p) $^2\Pi$ states depicted in Figure 7. These observations clarify qualitatively why the excitations to the red of the Al 3p → 3d line are stronger in one-photon (1_{uv}) excitation than those to the blue of the 3p → 4p line, which are stronger in two-photon (2_{vis}) excitation.

Analysis of the atomic Al compositions of the cluster electronic states calculated at their equilibrium structures indicates that the foregoing qualitative diatomic picture extends to some degree into the cluster spectra, as well. That is, when principal-axis coordinate systems in which the external-site Al atom falls on the major symmetry axes of the clusters are employed, analysis of the cluster ground-state wave functions

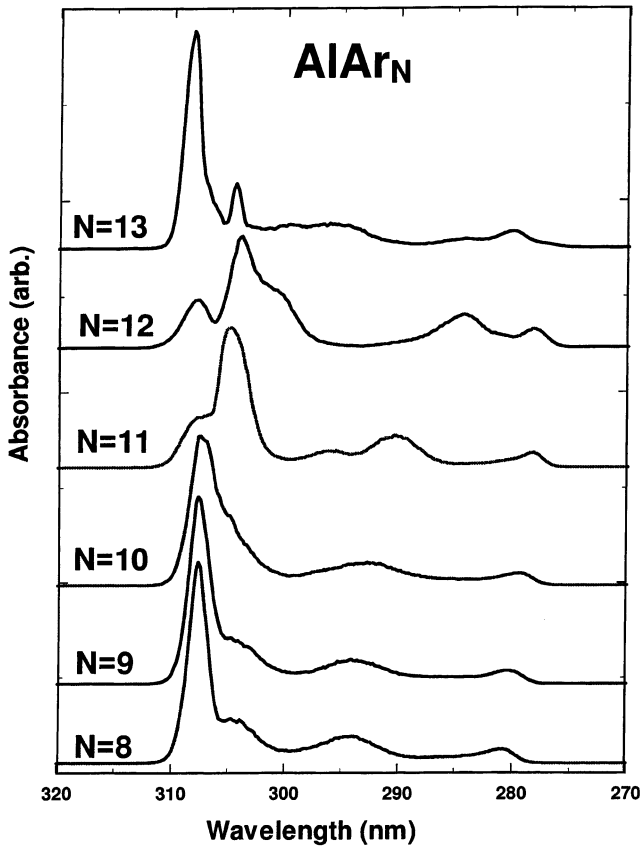

Figure 14. Theoretical one-photon ultraviolet absorption cross sections of $AlAr_N$ clusters ($N = 8-13$) calculated at 30 K, as discussed in the text. The N values chosen correspond to cluster spectra that are found to contribute by fragmentation to the measured Al^+Ar_6 multiphoton ionization spectrum of Figures 3 and 16.

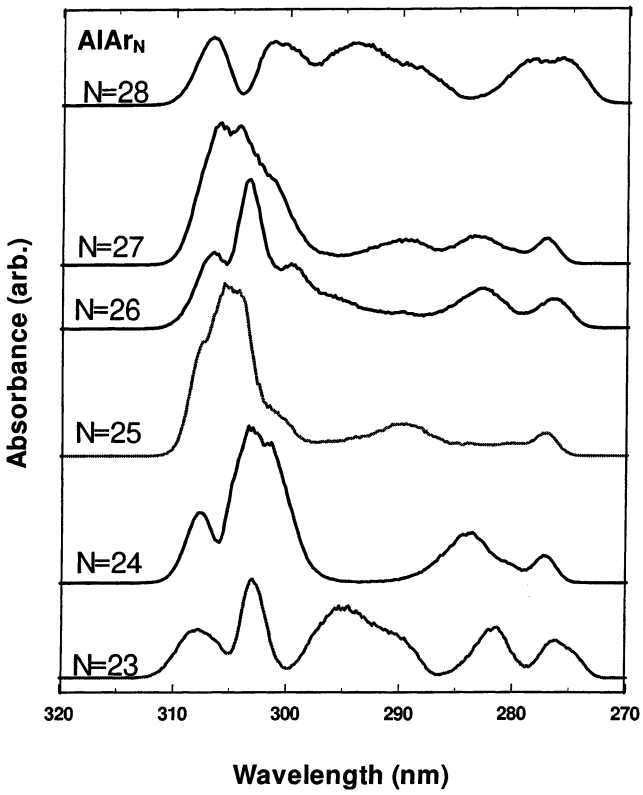

Figure 15. Theoretical one-photon ultraviolet absorption cross sections of $AlAr_N$ clusters ($N = 23-28$) calculated at 30 K, as discussed in the text. The N values chosen correspond to cluster spectra that are found to contribute by fragmentation to the measured Al^+Ar_{12} multiphoton ionization spectrum of Figures 3 and 16.

reveals excited electronic states that are quasi-diatomic Σ, Π, and Δ in nature, with the entire Ar_N aggregate playing the role of the "diatomic" partner. In this limit, avoided crossings in the cluster potential energy surfaces that arise from the underlying avoided crossing of the $^2\Pi$ and $^2\Sigma^+$ states depicted in Figure 6b can be regarded as accounting qualitatively for the overall intensity patterns depicted in the measured spectra of Figure 3. This quasi-diatomic circumstance is clearly related to the external-site location of the Al atom found from the quantitative results for all $AlAr_N$ clusters studied.

The red- and blue-shifted bands of Figure 4 are also accounted for qualitatively on basis of the foregoing quasi-diatomic model. Of course, the cluster electronic states obtained from diagonalization of the many-body Hamiltonian matrix of eqs 2 and 3 involve more generally mixing of all of the diabatic states derived from the diatomic states of Figures 5−7. It is nevertheless satisfying that the predicted and experimentally inferred orbital compositions of the complex energy states of the clusters are in general qualitative accord. Although it is convenient to speak of the cluster wave functions in terms of the atomic Al contributions alone, the many-electron spectral-product wave functions obtained from the Hamiltonian matrix of eqs 2 and 3 are derived from the diatomic functions, which are in turn obtained from the highly accurate MRCI calculations described above so, in fact, involve all electrons in the cluster of interest.

In Figures 14 and 15 are shown calculated ultraviolet absorption cross sections for the neutral clusters that contribute to formation of Al^+Ar_6 and Al^+Ar_{12} ions at 30 K, obtained following the development of section 3. These are seen to exhibit strong red bands and weaker blue bands, in general accord with the measured data of Figures 3 and 4 and with the foregoing qualitative remarks. Spectra at lower temperatures are found to be similar to those of Figures 14 and 15 but to have narrower spectral features, in accordance with the reduced effect of thermal excitations in the ground electronic states. The 30 K calculations evidently provide generally different spectral profiles as the size of the cluster changes from $N = 8$ to 13 and from 23 to 28, respectively, emphasizing again the individual molecular natures of the clusters. These differences are seen to be less significant among the three clusters $N = 8$, 9, and 10 in Figure 14, which correspondingly have similar radial distribution functions with approximately five Ar atoms in the nearest-neighbor shell (Figure 11). By contrast, the $N = 11$, 12, and 13 cross sections differ significantly from each other and from the smaller cluster results and also have different radial distribution functions. There are considerable differences among the cross sections for all of the clusters of Figure 15, although some limited degree of similarity is evident for $N = 25$ and 27. These two clusters correspondingly show somewhat similar radial distribution functions with approximately six Ar atoms in their nearest-neighbor shell (Figure 12). The calculated cross sections of Figures 14 and 15 all show considerable spectral structure over the entire wavelength range reported, consequent of the aforementioned strong interactions among the nearly degenerate excited-state potential energy surfaces arising from the 3d and 4p potential energy curves of Figures 5 and 6.

Although the calculated spectra show features well to the blue of the 303 nm 3p → 4p atomic Al line, the predicted absorption intensities to the red are evidently not shifted from the atomic 308 nm 3p → 3d Al line. The absence of strong red shifts in the cluster calculations is ultimately a consequence of the underestimate of the binding energies of the 3d and 4p diatomic

TABLE 3: Calculated Al^+Ar_N Cluster-Ion Fragmentation Coefficients[a,b]

	M							
N	5	6	7	8	9	10	11	12
8	0.996	0.004						
9	0.935	0.064						
10	0.285	0.715						
11	0.006	0.942	0.053					
12		0.081	0.874					
13		0.572	0.428					
14		0.066	0.832	0.103				
15		0.002	0.631	0.367				
16			0.260	0.736	0.005			
17				0.905	0.095			
18				0.083	0.857	0.060		
19				0.290	0.694	0.011		
20				0.038	0.913	0.049		
21					0.450	0.535	0.010	
22					0.038	0.540	0.365	0.047
23					0.027	0.715	0.231	0.027
24						0.107	0.621	0.262
25							0.095	0.860
26							0.014	0.871
27							0.001	0.735
28								0.137
29								0.042
30								0.007

[a] Fragmentation coefficients $F_{NM}^{(+)}$ of eqs 1 and 5 for production of cluster ions Al^+Ar_M from vibrationally excited parent ions Al^+Ar_N at 30 K, obtained following the theoretical development of section 3. The values shown, which are normalized to unity when summed over *M* for fixed *N*, include the effects of thermal evaporation during the thermal phase of the fragmentation process in addition to the prompt decays of the kinematical phase (Table 2) of the fragmentation process described in the text. [b] Entries not reported are judged too small ($<10^{-3}$) to contribute measureably to the fragmenation process.

potential energy curves shown in Figure 6b. These potential curves are accurate by most standards, but the absolute errors in the excited-state binding energies predicted relative to experimental values (~0.5−1.5%) are magnified in the cluster calculations by the presence of approximately six or more Ar nearest neighbors in each case (Figures 11 and 12), giving rise to somewhat larger absolute errors (~6 × 0.5% ≈ 3%) in the calculated cluster excitation energies. Inspection of the eigenspectra obtained from selected cluster configurations in the Monte Carlo simulations of the cross sections reveals the presence of low-lying red-shifted states, which, however, carry only small transtion intensities, with stronger transitions appearing to the blue of these states. Additionally, the small energy lowerings of the cluster ground states, which saturate at approximately -600 cm^{-1} with increasing cluster size, give rise to small blue shifts in the transition energies, which also contribute to the overall smaller red shifts in the calculations. Although the calculated potential energy curves can be individually adjusted to improve agreement with the diatomic spectra, these small offsets from experiment for the larger clusters are accommodated in the present development employing a uniform ad hoc shift in the wavelength scale of the calculated spectra.

To compare the calculated cross sections of Figures 14 and 15 with the measured spectra of Figure 3, eq 5 must be evaluated employing also the required shake-off coefficients and the prior distribution in the incident beam. In Table 3 are shown the calculated fragmentation coefficients for production of cluster ions for all of the neutral clusters of Figures 14 and 15. In contrast to the results of Table 2, which refer to prompt (≤1 ns) ionization only, the results of Table 3 include an additional one or two Ar atoms that evaporate during the thermal phase of the fragmentation process. These values are obtained from those of Table 2 and the distribution of excess internal vibrational energy available for additional fragmentation at the end of the kinematical phase of the simulation. Evidently, the entire fragmentation pattern of Table 3 is shifted to the left relative to that of Table 2, reflecting the production of smaller final cluster ions in Table 3 due to the additional thermal evaporation of Ar atoms not included in Table 2.

TABLE 4: Fragmentation and Prior Distribution Coefficients for $AlAr_N$ Clusters[a]

N	$F_{N6}^{(+)}$ [b]	P_N [c]	$F_{N6}^{(+)}P_N$ [d]	*N*	$F_{N12}^{(+)}$ [b]	P_N [e]	$F_{N12}^{(+)}P_N$ [d]
8	0.002			22	0.016		
9	0.026			23	0.009	0.793	0.244
10	0.292	0.224	0.210	24	0.088	0.065	0.195
11	0.385	0.429	0.530	25	0.288		
12	0.033			26	0.292	0.017	0.169
13	0.234	0.347	0.260	27	0.246	0.029	0.243
14	0.027			28	0.046	0.095	0.149
15	0.001			29	0.014		

[a] Values of coefficient appearing in eqs 1 and 5 for $M = 6$ and 12, obtained following the theoretical development of section 3. [b] Fragmentation coefficents of Table 3, renormalized to unity when summed over *N*. [c] Adjusted prior cluster beam distribution coefficients obtained by fitting theory and experiment for the Al^+Ar_6 cluster ion. Entries not reported do not contribute significantly to the production of Al^+Ar_6 ions by parent-ion fragmentation (Table 3). [d] Unity-normalized products of the indicated preceding two column entries. [e] As in footnote *c*, for Al^+Ar_{12} cluster ions.

The results of Table 3 have been employed to obtain the fragmentation coefficients for production of specific final ions Al^+Ar_M ($M = 6$ and 12) from the initial excited ions Al^+Ar_N shown in Table 4. These values are obtained directly from those of Table 3 by renormalizing the latter results to unity when summed over *N* for a given *M* values. The ranges of neutral clusters contributing to formation of Al^+Ar_6 ions ($N = 8-15$) and to Al^+Ar_{12} ions ($N = 22-30$) are evidently significant, although the primary contributions to Al^+Ar_6 are seen to be from $N = 10$, 11, and 13 and to Al^+Ar_{12} are from $N = 25$ to 27.

In the absence of prior knowledge of the incident neutral cluster distribution P_N required in eq 5, it is not possible to make ab initio predictions of the measured cluster-ion spectra. Although the calculated cluster energies of Figure 13 are suggestive, the actual composition of the incident molecular beam clearly depends on a number of additional factors associated with the operating characteristics of the laser ablation/pulsed molecular beam source. Accordingly, in the absence of a priori P_N values, composite spectra have been constructed from eq 5 employing two limiting prior distributions. The first of these is based on the assumption of uniformity in the incident neutral cluster beam (P_N = constant). Because only a limited number of neutral clusters in a finite range of *N* values contribute significantly to the formation of a given cluster ion (Table 3), this approximation should provide a reasonable first estimate of the distribution among these clusters. The second distribution, reported in Table 4, employs P_N values that have been arbitrarily adjusted to minimize the discrepancy between the experimental results and the calculated spectra obtained from eq 5. In this case, only those P_N values for the neutral clusters that contribute significantly (Table 4) to the composite spectra are included in the fitting procedure so that a relatively small number of values is involved in the adjustment. Of course, the measured spectra can also be fit employing an arbitrary number of neutral-cluster absorption cross sections. It is found, however, that such a procedure gives rise to unphysical (negative) P_N values, whereas the procedure employed here, in which the fragmentation

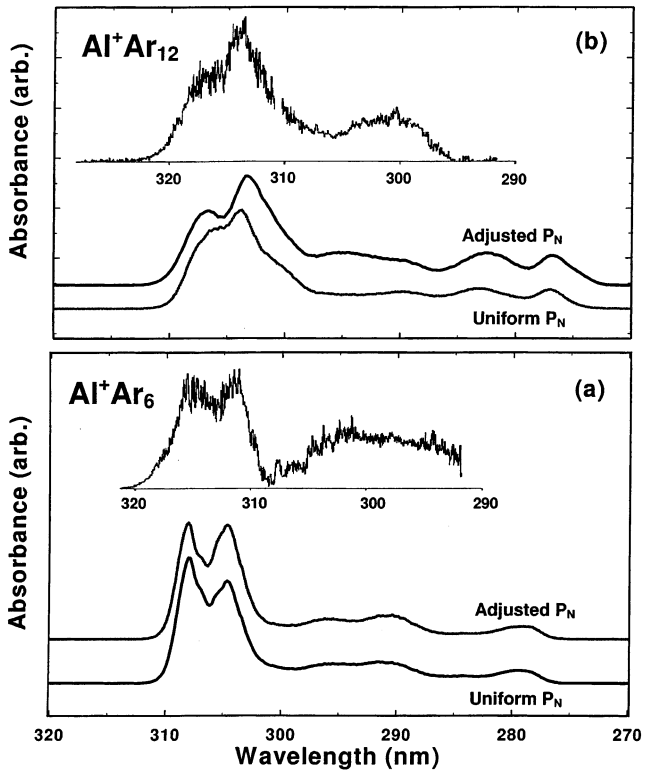

Figure 16. Experimental (a) Al^+Ar_6 and (b) $AlAr_{12}^+$ cluster-ion spectra from Figure 3 in comparison with calculated 30 K composite spectra constructed employing eq 5, the cross sections of Figures 14 and 15, the fragmentation coefficients of Table 3, and a uniform prior cluster beam distribution function (P_N = constant) or a prior cluster beam distribution (Table 4) adjusted to improve agreement between theory and experiment, as discussed in the text.

coefficients of Table 3 provide a guide to the cross sections to be included in the fitting, gives the positive P_N values of Table 4.

The $1_{uv} + 1_{vis}$ spectra for production of Al^+Ar_6 and Al^+Ar_{12} cluster ions of Figure 3 are reproduced in Figure 16, along with calculated composite action spectra obtained from eq 5 and the two approximations to the prior cluster distribution. Note that the wavelength scales of the experimental and calculated spectra have been offset by 6.5 and 10 nm for the Al^+Ar_6 and Al^+Ar_{12} cluster ions, respectively, to accommodate the underestimate of the calculated excited-state binding energies in Figure 6b. Evidently, the calculated spectral profiles of Figure 16 for Al^+Ar_6 and Al^+Ar_{12} cluster ions obtained employing a uniform prior distribution (P_N = constant) are in general accord with the measured spectra. In both cases, however, the intensities of the peaks to the red of the atomic lines are not reproduced in an entirely satisfactory manner by the calculations, and the overall intensity to the blue of the atomic lines is predicted to be somewhat weaker than that in the measured spectrum. Nevertheless, the calculations provide a quantitative and generally satisfactory accounting of the experimental spectra, suggesting that the theory can be employed with confidence in understanding the details of the measured data in terms of the underlying neutral cluster absorption cross sections and the parent cluster-ion fragmentation patterns.

Noticeable improvements are obtained between theory and experiment using the adjusted prior cluster beam distribution given in Table 4 with the relative intensities of the red peaks now in good accord with experiment and the blue portions of the calculated spectra now significantly more intense, also in accordance with the measurements. The fact that ad hoc adjustments in the prior neutral cluster distribution can lead to improvements between theory and experiment suggests that nonuniformity in the incident beam distribution must be included in a comprehensive accounting of the experiments. The particular range of P_N values of Table 4 inferred for the $M = 6$ cluster ion evidently corresponds to that of the more stable neutral clusters on the basis of the results of Figure 13b, whereas in the case of the $M = 12$ cluster ion, the $N = 23$ cluster appears to dominate the incident distribution in this cluster range. Although these adjusted P_N values are not unreasonable, additional theoretical and experimental considerations are clearly required to obtain definitive information on the incident neutral cluster distribution following the development reported here.

5. Discussion

The multiphoton ionization spectra of $AlAr_N$ clusters reported here are thought to arise from a complex sequence of excitation, ionization, and fragmentation processes inferred on the basis of the accompanying theoretical interpretation. Certain inferences can be drawn from the experimental data alone, however, whereas other conclusions follow from the theoretical predictions, with comparisons between the two sets of results providing additional confidence in the conclusions drawn. It is helpful to distinguish among these categories of information and inference and to describe more fully the limitations of the experimental and theoretical procedures on which they are based to provide a better understanding of the conclusions that can be unambiguously drawn from the present study.

The resonant $1_{uv} + 1_{vis}$ mass spectrum of Figure 2 shows an abundance of smaller ($M \leq 12$) cluster ions detected relative to larger ones and also reveals somewhat enhanced abundances at selected mass values, apparently associated with major and minor icosahedral magic numbers.[39] In the absence of significant parent-ion cluster fragmentation, the mass spectrum would reflect the neutral cluster distribution directly, in which case the enhanced magic-number abundances suggest that the neutral clusters are icosahedral in nature. By contrast, in the presence of significant parent-ion fragmentation, the magic-number clusters in the mass spectrum would presumably more closely reflect the stabilities of icosahedral-like fragment cluster ions produced. Previously reported $AlAr_N$ cluster studies employing single-photon ionization also show icosahedral enhancements in mass spectra.[10,11] These observations are interpreted to suggest that the magic-number signals reflect stabilities in the neutral $AlAr_N$ distribution, rather than in the ionic clusters, on the basis of the apparent absence of cluster fragmentation in the field-free region of the time-of-flight mass spectrometer employed. That is, the previously reported measurements suggest that parent-ion fragmentation can be eliminated in the threshold regions of the cluster-ion appearance potentials, at least for the smaller clusters ($N < 30$).[10,11] However, such observations only measure processes occurring in the approximate time interval $10^{-3} > \tau > 10^{-7}$ s so do not rule out the occurrence of more prompt fragmentations for all clusters. Consequently, it seems likely that the spectrum of Figure 2 can include cluster-ion abundances that derive in whole or in part from parent-ion fragmentation.

Figure 3 shows strong red- and weaker blue-shifted features in the $1_{uv} + 1_{vis}$ spectra, whereas the intensities of the red and blue bands are reversed in the $2_{vis} + 1_{vis}$ spectra. These results can be attributed to perturbed dipole-allowed and -forbidden $3p \rightarrow 3d$ and 4p atomic Al excitations, respectively, in accordance with the natures of the 3d and 4p AlAr diatomic potential energy curves.[19] The intensities of the red- and blue-

shifted bands for the larger clusters in the $1_{uv} + 1_{vis}$ spectra of Figure 4 are similarly clarified on this basis. The observation of *red-shifted* bands associated with the dipole-allowed 3p → 3d electronic excitation, which increase slowly to the red with increasing cluster size (Figure 4), is striking in view of the appearance of only *blue-shifted* bands in the matrix isolation studies reported to date.[4−7] The failure of the observed 3p → 3d and 4p cluster spectra of Figures 3 and 4 to converge to the reported bulk behavior,[4−7] as well as observations of similar nonconvergence of 3p → 4s excitations in $AlAr_N$ clusters,[11] strongly suggests that the Al trapping sites in these clusters are generally different than those in the bulk matrix.[15,22]

Stabilization of the 3d state relative to the 3p ground state is consistent with the Al atom occupying external sites on Ar_N cluster. Blue shifts of electronic dopant spectra are generally attributed to repulsive interactions of the excited electronic state confined to the initial matrix cage geometry. By contrast, a significant red shift might be expected upon excitation to the lowest spin−orbit 3d state of a surface-bound Al atom, given the much stronger binding energy of the (3d) $^2\Delta$ AlAr diatomic potential ($D_e = 525$ cm^{-1}) relative to that of the ground-state potential reported in Figure 6. Furthermore, the very gradually increasing red and blue shifts observed with increasing cluster size in Figure 4 also suggest that external Al sites are highly probable. Internal sites, by contrast, are expected to give rise to *rapidly* increasing blue shifts with cluster size to limiting values rather than to the more gradual behavior of Figure 4. The relatively broad spectral bands reported in Figures 3 and 4 also suggest a somewhat greater diversity of trapping sites, which would be more readily accessible by thermally induced Al atom mobility on the surfaces of clusters than might be expected from Al atoms trapped internally. Internal trapping sites would also be expected to give rise to narrower bands, as is observed in the matrix-isolation studies.[4−7] Of course, the possibility of both external and internal trapping sites, giving rise to red and blue shifts, respectively, cannot be ruled out entirely on the basis of experiments alone. Nevertheless, the failure of the measured spectra in $AlAr_N$ to converge to values observed in bulk matrix isolated studies strongly support the conclusion that the Al trapping sites in these clusters are most likely external rather than internal to the clusters.

Uncertainties in the observed spectra could result from a number of potential sources, including the need to concatenate spectra from the shorter spectral scans involving different laser dyes. These individual scans could also be susceptible to variations in cluster source, probe laser, and other conditions over short and long time scales. Specifically, shot-to-shot variations can arise from the probe laser, an effect that is amplified by the use of nonlinear crystals for ultraviolet generation. Additionally, pulse-to-pulse variations in the Al ablation cluster source associated with pulsed-valve performance, changes in Al rod surface characteristic and in the gas flow through the apparatus, and fluctuations in the ablation laser power that contribute to short time scale uncertainties in the spectra are judged to be primarily responsible for the apparent fine structure in the individual scans obtained.

In some cases, significant noise at the ends of adjacent dye intervals leads to the absence of overlap of data, precluding accurate matching of intensities between the two data sets. Slope matching aids in bringing the separate scans into alignment in these cases. Such gaps in the spectral segments give rise to uncertainty primarily in the overall relative magnitudes of the red- and blue-shifted bands and not in the strutures within the bands, possibly accounting for some of the remaining discrepancy between theory and experiment in Figure 16. On a longer time scale, issues arise concerning separate experiments performed on separate days with different dye mixtures and different optical alignments. To resolve these possible uncertainties, complete scans were repeated in selected cases (including $N = 12$) and found to be highly reproducible, suggesting that experimental conditions could be held constant over periods of many months.

Although some spectral broadening due to saturation of narrow absorption features could be anticipated, it is unlikely that the ultraviolet laser fluences used in the $1_{uv} + 1_{vis}$ experiment are sufficient to saturate the broad 3p → 3d and 4p excitations of interest. This view is supported by the linearity in I_{uv} of the measured $1_{uv} + 1_{vis}$ signals. Combinations of weak internal conversion, intersystem crossing, and fluorescence decay from the intermediate excited states are unlikely to compete with the ionization step in view of the relatively high visible power employed (∼10−50 mJ/5 ns pulse), although strong internal conversion, neutral fragmentation, or relaxation to the 4s state cannot be ruled out. Furthermore, because the signals were not normalized to the visible ionizing fluence, they do not take into account possible variations in the ionization cross sections of the intermediate cluster states or in the visible laser power, leading to possible uncertainties in the individual spectral scans. The large photoionization cross sections of the clusters near threshold, however, estimated to be $\sim 10^{-17}$ cm^2 on the basis of atomic Al 3d and 4p values (S. T. Manson, private communication), suggest that the ionizing step is saturated, in accord with the experimental observation. The variations in the cross sections amount in any event to a 10−20% decrease with increasing laser frequency over the spectral range of the visible scans performed (∼660−580 nm). Similarly, the visible laser fluence, which is obtained directly from the residual undoubled dye laser fundamental, was kept relatively constant over the intervals of the individual spectral scans. Accordingly, spectral variations in the photoionization process are judged unlikely to affect significantly the recorded spectra.

The results of the theoretical calculations largely confirm the foregoing conclusions of external Al trapping sites and likely parent-ion fragmentation, and provide additional quantitative structural and spectroscopic information. The low-temperature structures of Figures 8−10 illustrate the propensity of the Al atom to assume an external location in the structures studied ($N \leq 54$). In some cases, the Al atom assumes a cap-site location and is incorporated into an icosahedral-like structure, as in Figures 9 and 10, whereas in other cases the geometry is more complex. The radial distribution functions of Figure 11 for the smaller clusters reflect thermal effects associated with vibrational motions of individual molecules, whereas those of Figure 12 for the larger clusters involve transitions among thermally accessible isomers, as well. This diversity of structures is clearly a consequence of the spin−orbit-split anisotropic nature of the ($^2P_{1/2}$)Al−($^1S_0$)Ar interactions and of the comparable strength of the Ar−Ar mutual attractions. Previously reported theoretical studies of BAr_N clusters, which employ anisotropic ($^2P_{1/2}$)B−($^1S_0$)Ar interaction potentials, also report complex cluster geometries with the B atom residing in an external site in all cases considered.[18]

In contrast to the neutral clusters, the structures of the ionic clusters of Figures 8−12 are qualitatively similar to those of icosahedral rare-gas clusters,[39] with the Al^+ ion external to the clusters in some cases (Figure 8) and internal (Figure 10) in other cases for the smaller clusters, but uniformly internal for the larger clusters ($N > 12$). The significant differences between

the neutral and parent-ion cluster geometries for all but the smallest clusters give rise to generally large differences between the calculated vertical and adiabatic ionization potentials, reported in Table 1, and to significant prompt and weak thermal parent-ion fragmentation, as reported in Tables 2 and 3. These theoretical results support the conclusion that the icosahedral mass enhancements of Figure 2 and those of previously reported Al^+Ar_M mass spectra[10,11] reflect the stabilities of the cluster ions rather than of the neutrals. Additionally, the predicted weak thermal evaporation of Ar atoms is in accord with the fragmentation measurements made on an appropriately long (microsecond to millisecond) time scale.[11] Further theoretical support of this contention is provided by the total neutral and cluster-ion energies of Figure 13, which suggest that the ionic clusters reflect icosahedral stabilities to a greater degree than do the neutral clusters. The previously measured appearance potentials,[10,11] tabulated in Table 1, are also in accord with these conclusions and are in very good agreement with the calculated vertical ionization potentials when the role of parent-ion fragmentation is taken into account.

The calculated neutral cluster ultraviolet absorption cross sections of Figures 14 and 15 show bands to the red and blue of the atomic Al 3p → 3d and 4p lines that are quite structured and that have intensity distributions in general accord with the experimental spectra of Figures 3 and 4. These broad bands, which are evidently sensitive in their detailed features to the particular cluster considered, can be attributed to the interactions among the neutral-cluster potential energy surfaces that derive from the 3p → 3d and 4p potential energy curves of Figures 5−7 when employed in the Hamiltonian matrix of eqs 2 and 3. The calculated composite cross sections for Al^+Ar_6 and Al^+Ar_{12} ions obtained from eq 5 employing the fragmentation coefficients of Table 3 are seen in Figure 16 to be in good agreement with the corresponding measured action spectra. The predicted relative intensities of the two red peaks in the Al^+Ar_6 spectrum are in general agreement with experiment employing a uniform neutral cluster distribution and in excellent accord with the data when the adjusted distribution of Table 4 is employed. Similarly, the red bands in the calculated Al^+Ar_{12} composite cross section employing both uniform and adjusted neutral cluster distributions are in accord with experiment, the latter providing noticeably improved agreement. In both cluster-ion cross sections, the predicted blue band intensities are somewhat weaker than the measured values, the adjusted prior distribution providing improved results.

Calculations performed in the absence of parent-ion cluster fragmentation give cross sections that are in generally poor agreement with the measured spectra. The predicted $AlAr_6$ absorption cross section, for example, bears no resemblance by itself to the experimental spectrum of Figure 16, and the calculated cross sections generally do not include the broad flat blue bands evident in Figure 4.[33] Although all of the cross sections show red bands in approximately the same spectral interval and in one or two cases there is a hint of agreement between theory and experiment in this interval (cf. the $N = 12$ results of Figures 14 and 16), the predicted blue bands appear as isolated features in the individual cross sections. It is only in combinations predicted by eq 5 employing the fragmentation coefficients of Table 3 that the calculations give broad blue bands that are in accord with the experimental spectra over the entire measured interval. It can be concluded that parent-ion cluster fragmentation plays an important role in the photoexcitation and ionization of $AlAr_N$ clusters.

Approximations made in the theoretical formalism and calculations performed can affect the reliability of the predicted results. The theory underlying the Hamiltonian matrix of eqs 2 and 3 incorporates a number of diatomic-based procedures that have a long history of successful application in various contexts[25,34,35] particularly in connection with anisotropic interactions.[41,43−46] Accordingly, the reliability of the predicted structures of Figures 8−12 depends primarily on the quality of the diatomic calculations reported in Figures 5−7. These results are in satisfactory accord with available AlAr experimental data, providing considerable confidence in the results of the MRCI calculations performed and suggesting that the cluster structure predictions are similarly reliable.

The transformation matrix employed in eq 4 in constructing the atomic-product representation central to the development contributes primarily to the excited electronic states that arise from the nearly degenerate 3p → 3d and 4p Al atom transitions. Use of the dipole transition moment matrix in constructing the transformation matrix rather than the invariant one-electron transition density matrix introduces a possible source of error in the calculated absorption cross sections. However, in view of the weak van der Waals nature of Al−Ar interactions, this approximation is expected to be vaild except for very small Al−Ar interatomic separations, which are not highly sampled in the Monte Carlo procedures.[26,27] The approximate invariance of other one-electron operators has long been used to define and construct diabatic states in related contexts.[31,47−49]

The dynamical simulations of cluster-ion fragmentation are based on well-known theoretical procedures,[50] so the reliability of predicted fragmentation coefficients depends largely on the quality of the potential energy surfaces employed. Although the ground-state surfaces are expected to be satisfactory, as indicated above, the ionic surfaces do not include the self-consistent effects of Ar−Ar interactions due to dipole and other moments induced by the Al^+ ion. Additionally, the initial conditions for parent-ion dissociation are based on sampling made on the ground-state cluster energy surfaces, largely ignoring the role of the intermediate electronically excited states in this connection. These self-consistent polarization effects apparently have little effect on the ionic cluster energies, however, as is suggested by the very good agreement between the calculated vertical ionization potentials and the measured appearance potentials.[10,11] Similarly, although some motion can take place on the intermediate excited-state cluster potential energy surfaces on the ∼5 ns time scale of the ionizing visible laser pulse, the shallow natures of the potential surfaces should ensure that there is little cluster reorganization during the $1_{uv} + 1_{vis}$ or $2_{vis} + 1_{vis}$ processes.

Finally, in the absence of a priori knowledge of the neutral cluster distribution (P_N) produced by the pulsed molecular beam source, predictions of the action spectra for production of a specific cluster ion from eqs 1 and 5 are precluded. Adoption of a uniform neutral distribution in this connection, although unrealistic for the entire range of cluster sizes produced, is clearly reasonably over the relatively narrow ranges of N values that contribute by fragmentation (Table 4) to the cluster-ion action spectra reported in Figure 16. Moreover, ad hoc adjustment of the P_N values for these neutral clusters provides improved agreement between theory and experiment and is seen to result in only modest changes in the weighting coefficents for the Al^+Ar_6 cluster ion (cf. $F_{N6}^{(+)}$ and $F_{N6}^{(+)}P_N$ values in Table 4), whereas somewhat more significant changes are apparent in the case of the Al^+Ar_{12} cluster-ion spectrum. These results suggest that there is an opportunity to investigate the nature of the prior cluster distribution from a combined theoretical and

experimental approach, which will require additional studies of the absorption cross sections, fragmentation coefficients, and other attributes of a greater range of smaller and larger clusters.

Acknowledgment. This work was supported in part by grants from the US Air Force Office of Scientific Research (Grants F49620-92-J-0537 and F49620-93-I-0326) under the auspices of the High Energy Density Matter Program administered by Dr. Michael Berman, by a National Science Foundation Fellowship for J.M.S., and by National Research Council Senior and Summer Fellowships and other support from AFOSR and the Air Force Research Laboratory for P.W.L. and R.J.H. We thank Drs. Mario E. Fajardo and Jeffrey D. Mills for helpful collaboration and ongoing comments during the course of the investigation and Professor S. T. Manson for providing Hartree−Slater estimates of the atomic Al 3d and 4p photoionization cross sections.

References and Notes

(1) Vegard, L. *Nature* **1924**, *114*, 357−359.

(2) Myer, B. *Low Temperature Spectroscopy*: *Optical Properties of Molecules in Matrixes, Mixed Crystals, and Frozen Solutions*; American Elsevier: New York, 1971.

(3) *Chemistry and Physics of Matrix-Isolated Species*; Andrews, L., Moskovits, M., Eds.; North-Holland: Amsterdam, 1989.

(4) Ammeter, J. H.; Schlosnagle, D. C. *J. Chem. Phys.* **1973**, *59*, 4784−4820.

(5) Grinter, R.; Stern, D. R. *J. Mol. Struct.* **1982**, *80*, 147−150.

(6) Abe, H.; Kobe, D. M. *Ber. Bunsen-Ges. Phys. Chem.* **1983**, *87*, 523−527.

(7) Grinter, R.; Singer, R. J. *Chem. Phys.* **1987**, *113*, 87−97.

(8) Hebert, T.; Schriever, U.; Kolb, D. M. *Chem. Phys. Lett.* **1992**, *200*, 258−262.

(9) Hui, Q.; Perssen. J. L.; Beijersbergen, J. H.; Takami, M. *Z. Phys. B* **1995**, *98*, 353−357.

(10) Schriver, K. E.; Hahn, M. Y.; Persson, J. L.; LaVilla, M. E.; Whetten, R. L. *J. Phys. Chem.* **1989**, *93*, 2869−2871.

(11) Whetten, R. L.; Schriver, K. E.; Persson, J. L.; Hahn, M. Y. *J. Chem. Soc., Faraday Trans.* **1990**, *86*, 2375−2385.

(12) Reho, J. H.; Merker, U.; Radcliff, M. R.; Lehmann, K. K.; Scoles, G. *J. Phys. Chem. A* **2000**, *104*, 3620−3626.

(13) Yang, X.; Dagdigian, P. J. *J. Chem. Phys.* **1998**, *109*, 8920−8928. Tan, X.; Dagdigian, P. J.; Alexander, M. H. *Faraday Discuss.* **2000**, *118*, 387−404. Tan, X.; Dagdigian, P. J.; Williams, J.; Alexander, M. H. *J. Chem. Phys.* **2001**, *114*, 8938−8946. Tan, X.; Dagdigian, P. J. *Chem. Phys.* **2002**, *283*, 5−16.

(14) Fajardo, M. E.; DeRose, M. E.; Tam, S. Aluminium Doped Parahydrogen Solids. In *Proceedings of the High Energy Density Matter Contractor's Conference*; Berman, M. R., Ed.; 2000, p 26. Fajardo, M. E.; Tam, S.; Thompson, T. L.; Cordonnier, M. E. *Chem. Phys.* **1994**, *189*, 351−364.

(15) Spotts, J. M.; Wong, C.-K.; Johnson, M. S.; Okumura, M. Resonant Multiphoton Ionization Spectroscopy of $Al(Ar)_N$ Clusters. In *Proceedings of the High Energy Density Matter Contractor's Conference*; Carrick, P. G., Williams, N. T. Eds.; 1997; PL-TR-96-3037, pp 69−75.

(16) Li, X.; Hahn, M. Y.; El-Shall, M. S.; Whetten, R. L. *J. Phys. Chem.* **1991**, *95*, 8524−8528.

(17) Stienkemeier, F.; Higgins, J.; Callegari, C.; Kanorsky, S. I.; Ernst, W. E.; Scoles, G. *Z Phys. D* **1996**, *38*, 253−263. Higgins, J.; Callegari, C.; Reho, J.; Stienkemeier, F.; Ernst, W. E.; Gutowski, M.; Scoles, G. *J. Phys. Chem. A* **1998**, *102*, 4952−4965.

(18) Gregurick, S. K.; Hartle, B.; Alexander, M. H. *J. Chem. Phys.* **1996**, *104*, 2684−2691.

(19) Gardner, J. M.; Lester, M. I. *Chem. Phys. Lett.* **1987**, *137*, 301−305. Callender, C. L.; Mitchell, S. A.; Hackett, P. A. *J. Chem. Phys.* **1989**, *90*, 5252−5261. McQuaid, M. J.; Gole, J. L.; Heaven, M. C. *J. Chem. Phys.* **1990**, *92*, 2733−2739. Heidecke, S. A.; Fu, Z.; Colt, J. R.; Morse, M. D. *J. Chem. Phys.* **1992**, *97*, 1692−1710.

(20) Aziz, R. A.; Slaman, M. J. *J. Mol. Phys.* **1986**, *58*, 679−697.

(21) Estrin, D. A.; Liu, L.; Singer, S. J. *J. Phys. Chem.* **1992**, *96*, 5325−5331.

(22) Spotts, J. M. Ph.D. Dissertation, California Institute of Technology, Pasadena, CA, 1998.

(23) Spotts, J. M.; Wong, C.-K.; Johnson, M. S.; Okumura, M.; Sheehy, J. A.; Boatz, J. A.; Langhoff, P. W. Experimental and Theoretical Characterization of the $X^2\Pi_{1/2}(3p) \rightarrow G^2\Sigma^+(4p)$ Bound-to-Continuum Transition in AlAr. *J. Chem. Phys.*, submitted for publication.

(24) Jellenik, J. *Theory of Atomic and Molecular Clusters*; Springer: Berlin, 1999. Johnson, R. L. *Atomic and Molecular Clusters*; Taylor and Francis: London, 2002.

(25) Langhoff, P. W. *J. Phys. Chem.* **1996**, *100*, 2974−2984.

(26) Boatz, J. A.; Fajardo, M. E. *J. Chem. Phys.* **1994**, *101*, 3472−3487. Fajardo, M. E.; Boatz, J. A. *J. Comput. Chem.* **1996**, *18*, 381−392.

(27) Boatz, J. A.; Sheehy, J. A.; Hinde, R. J.; Langhoff, P. W. Quantum and Classical Monte Carlo and Molecular Dynamics Simulations of the Structures, Photoionization-Induced Fragmentation, and Optical Absorption Spectra of $AlAr_N$ Clusters. In *Proceedings of the High Energy Density Matter Contractor's Conference*; Berman, M. R., Ed.; Cocoa Beach, FL, 1999; pp 111−1218.

(28) Werner, H.-J.; Meyer, W. J. *J. Chem. Phys.* **1981**, *74*, 5802−5807.

(29) Moore, C. E. *Atomic Energy Levels*; NBS Circular 467; U.S. Government Printing Office: Washington, DC, 1949.

(30) Nikitin, E. E. *J. Chem. Phys.* **1965**, *43*, 744−750. Aquilanti, V.; Grossi, G. *J. Chem. Phys.* **1980**, *73*, 1165−1172.

(31) Lefebvre-Brion, H.; Field, R. W. *Perturbations in the Spectra of Diatomic Molecules*; Academic: New York, 1986.

(32) Edmonds, A. R. *Angular Momentum in Quantum Mechanics*; Princeton University Press: Princeton, NJ, 1957.

(33) Boatz, J. A.; Sheehy, J. A.; Langhoff, P. W. Monte Carlo Simulations of the Structures and Optical Absorption Spectra of $AlAr_N$ Clusters. In *Proceedings of the High Energy Density Matter Contractor's Conference*; Berman, M. R., Ed.; Monterey, CA, 1998; pp 84−101.

(34) Baylis, W. E. *J. Chem. Phys.* **1969**, *51*, 2665−2679. Sando, K.; Erickson, G. J.; Binning, R. C., Jr. *J. Phys. B: At. Mol. Phys.* **1979**, *12*, 2697−2705.

(35) Dawson, J. F.; Balling, L. C. *J. Chem. Phys.* **1979**, *71*, 836−842. Balling, L. C.; Wright, J. J. *J. Chem. Phys.* **1983**, *79*, 2941−2944.

(36) Langhoff, P. W.; Hinde, R. J.; Boatz, J. A.; Sheehy, J. A. *Chem. Phys. Lett.* **2002**, *358*, 231−236.

(37) Langhoff, P. W.; Boatz, J. A.; Hinde, R. J.; Sheehy, J. A. In *Low-Lying Potential Energy Surfaces*; Hoffmann, M. R., Dyall, K. G., Eds.; ACS Symposium Series 828; American Chemical Society: Washington, DC, 2002; pp 221−237.

(38) Barnett, R. N.; Reynolds, P. J.; Lester, W. A., Jr. *J. Comput. Phys.* **1991**, *96*, 258−276.

(39) Mackay, A. L. *Acta Crystallogr.* **1962**, *15*, 916−918.

(40) Partridge, H.; Bauschlicher, C. W., Jr.; Visscher, L. *Chem. Phys. Lett.* **1995**, *246*, 33−39.

(41) Tutin, A. B.; Mayne, H. R. *J. Chem. Phys.* **1998**, *108*, 308−316.

(42) Bartlett, R. J.; Stanton, J. F. In *Reviews in Computational Chemistry*; Lipkowitz, K. B.; Boyd, D. B., Eds.; VCH: New York, 1994; pp 65−169.

(43) Lawrence, W. G.; Apkarian, V. A. *J. Chem. Phys.* **1994**, *101*, 1820−1831.

(44) Naumkin, F. Yu.; Knowles, P. J.; Murrell, J. N. *Chem. Phys.* **1995**, *193*, 27−36.

(45) Cheng, E.; Whaley, K. B. *J. Chem. Phys.* **1996**, *104*, 3155−3175.

(46) Kuntz, P. J. *Chem. Phys.* **1999**, *240*, 19−38.

(47) Rebentrost, F.; Lester, W. A., Jr. *J. Chem. Phys.* **1975**, *63*, 3737−3740; *J. Chem. Phys.* **1976**, *64*, 3879−3884.

(48) Alexander, M. H. *J. Chem. Phys.* **1993**, *99*, 6014−6026; **1998**, *108*, 4467−4477.

(49) Williams, J.; Alexander, M. H. *J. Chem. Phys.* **2000**, *112*, 5722−5730.

(50) Suhm, M. A.; Watts, R. O. *Phys. Rep.* **1991**, *204*, 293−329.